Challenges in constraining gravity with cosmic voids

Christopher Wilson and Rachel Bean
Department of Physics, Cornell University, Ithaca, New York 14853, USA
and Department of Astronomy, Cornell University, Ithaca, New York 14853, USA

(Received 19 December 2022; accepted 20 April 2023; published 7 June 2023)

We compare void size and clustering statistics for nDGP and $f(R)$ gravity models and general relativity (GR) using N-body simulations. We show how it is critical to consider the statistics derived from mock galaxy catalogs rather than the dark matter halos alone. Marked differences between the void size functions for GR and $f(R)$ models which present when voids are identified using dark matter halos are removed when voids are identified, more realistically, from mock galaxy tracers of the halos. The void radial velocities and velocity dispersions in the $f(R)$ and nDGP models are enhanced relative to GR in both halos and mock galaxy identified voids. Despite this, we find that the redshift space void quadrupole moments derived from the mock galaxy tracers are strikingly similar across the three gravity models. The Gaussian streaming model (GSM) is shown to accurately reconstruct ξ_2 in modified gravity models, and we employ the GSM, using a functional derivative approach, to analyze the insensitivity of ξ_2 to the gravity model. Assuming linear theory, we show the void quadrupole to be an unbiased estimator of the redshift space growth rate parameter $\beta = f/b$ in the modified gravity theories.

DOI: 10.1103/PhysRevD.107.124008

I. INTRODUCTION

A century after Einstein dismissed the inclusion of a cosmological constant, Λ, in his field equations, such a term, equivalent to the addition of a nonzero vacuum energy, has since become the default explanation for the observed accelerated cosmic expansion [1–9]. When the observationally inferred vacuum energy $\Lambda_{\rm obs}$ is compared against theoretical calculations from quantum field theory, however, there is a discrepancy of 120 orders of magnitude, leading to the cosmological constant problem. This incredible fine-tuning has led to the consideration of alternative theoretical explanations for the observations.

One avenue of investigation is to induce deviations from general relativity (GR) through the inclusion of new scalar degrees of freedom (see, for example, [10]). These new gravitational degrees of freedom, referred to as the "fifth force," typically lead to deviations from GR on cosmic scales $\sim 1/\Lambda_{\rm obs}$. General relativity is incredibly successful at predicting gravity on Solar System scales. Hence, to remain viable, modified gravity theories must pass a plethora of strict Earth and Solar System scale tests [11]. Theories which retain viability typically feature "screening" mechanisms which suppress fifth-force modifications, and restore general relativity, in Solar System–like environments.

In Hu-Sawicki $f(R)$ gravity [12], the "chameleon" mechanism [13,14] acts to increase the mass of the scalar field which mediates the additional fifth force in regions of high density, leading to a lack of propagation and suppression. Other alternative theories such as Dvali-Gabadadze-Porrati (DGP) gravity [15] rely on the "Vainshtein" mechanism [16], which suppresses the fifth force whenever the derivatives of the additional scalar field grow large, such as inside and immediately surrounding a large overdense region. While these screening mechanisms suppress modifications to GR in high-density environments, potential modifications to gravity would be expected to arise in cosmic voids, which are large underdense regions of the cosmic web.

Cosmic voids have been observed in a wide range of cosmological surveys including photometric galaxy surveys (e.g., Dark Energy Survey [17]), spectroscopic galaxy surveys (e.g., SDSS/eBOSS [18,19]), and cosmic microwave background (CMB) surveys (e.g., Planck [20]). Voids can have a direct impact on weak gravitational lensing [21–29], redshift space distortions [30–41], CMB lensing [25,42,43], the integrated Sachs-Wolfe effect [44–49], and the kinetic Sunyaev-Zel'dovich effect [50] among others. Upcoming galaxy surveys such as Euclid [51], the Dark Energy Spectroscopic Instrument (DESI) [52,53], the Vera Rubin Large Synoptic Survey Telescope [54], Roman Space Telescope [55], and CMB surveys such as the Simons Observatory [56] and CMB-S4 [57] promise to add a wealth of cosmological data for void analyses.

Voids have been considered in the study of dark energy models [58–72] and as probes of massive neutrinos [73–76]. The use of voids to identify potential modifications to gravity has been considered for a variety of models including nDGP, $f(R)$, symmetron, and Galileon models [77–89].

In previous work [78], we showed that in $f(R)$ modified gravity scenarios, the fifth force leads to an enhancement to the void's coherent radial velocity profile—the magnitude

 © 2023 American Physical Society

of which is dependent on the size of the void itself. While the radial velocity is not directly observable in itself, it does effect observable redshift space distortion statistics within the void environment.

In this paper we consider the effects induced by modifications to gravity on the void size function and on the redshift space void quadrupole moment to assess whether these effects might be observationally measurable. We also consider the application of the measured void quadrupole to recover a measure of the linear growth rate in the modified gravity theories, by constraining $\beta = f/b$, where f is the cold dark matter (CDM) linear growth rate and b is the bias of the observed tracers, as considered for GR in [33], and similarly in [40,90].

This paper is structured as follows. Section II lays out the formalism. In Sec. III, we present our main results centered around the measurable void statistics in modified theories of gravity. These findings are analyzed and contextualized in Sec. IV. They are also used to determine potential constraints on β derived from the void quadrupole. In Sec. V we present the conclusions and implications of this work for future research.

II. FORMALISM

In Sec. II A, we describe the two different modified gravity models, $f(R)$ and nDGP gravity, to be compared with the baseline ΛCDM model in this work. The choice of N-body simulations and application of halo occupation distribution (HOD) is outlined in Sec. II B. The void finding and void stacking procedures are described in Secs. II C and II D, respectively. Finally, the Gaussian streaming model is summarized in Sec. II E.

A. Modified gravity models

1. $f(R)$ gravity

We modify the standard Einstein-Hilbert action [91] to instead take the form

$$S_{f(R)} = \int d^4x\sqrt{-g}\left(\frac{1}{16\pi G}[R + f(R)] + \mathcal{L}_m(\psi_i)\right), \quad (1)$$

where f is some function of the Ricci scalar R and $\mathcal{L}_m(\psi_i)$ is the standard model matter Lagrangian composed of fields ψ_i. In this paper, we consider the $f(R)$ form specified by Hu and Sawicki [12],

$$f(R) = -m^2\frac{c_1(R/m^2)^n}{c_2(R/m^2)^n + 1}. \quad (2)$$

Here $m = H_0\sqrt{\Omega_{m0}}$ is a characteristic mass scale, with H_0 the Hubble constant, Ω_{m0} the fractional matter energy density today and free parameters c_1, c_2, and n that are specified to fully define $f(R)$.

The modified field equations are obtained by varying the action with respect to the metric $g_{\mu\nu}$:

$$G_{\mu\nu} + f_R R_{\mu\nu} - g_{\mu\nu}\left[\frac{1}{2}f(R) - \Box f_R\right] - \nabla_\mu\nabla_\nu f_R = 8\pi G T_{\mu\nu}. \quad (3)$$

Here $G_{\mu\nu}$ is the Einstein tensor $G_{\mu\nu} = R_{\mu\nu} - \frac{1}{2}g_{\mu\nu}R$, with $R_{\mu\nu}$ the Ricci tensor, $\Box = g^{\mu\nu}\nabla_\nu\nabla_\mu$ with ∇_μ the standard covariant derivative with respect to $g_{\mu\nu}$, and $f_R \equiv \frac{df(R)}{dR}$.

In the limit of high curvature, f_R is given by

$$f_R \simeq -n\frac{c_1}{c_2^2}\left(\frac{m^2}{R}\right)^{n+1}. \quad (4)$$

In order to match the observed expansion history, $\bar{R}$ must remain unchanged from its ΛCDM value, which gives

$$\bar{f}_R \simeq -\frac{nc_1}{c_2^2}\left[3\left(\frac{1}{a^3} + 4\frac{\Omega_{\Lambda 0}}{\Omega_{m0}}\right)\right]^{-(n+1)}. \quad (5)$$

This expansion history matching condition also fixes the ratio $\frac{c_1}{c_2} \approx 6\frac{\Omega_{\Lambda 0}}{\Omega_{m0}}$, as shown in [12], leaving two free model parameters: $\frac{c_1}{c_2^2}$ and n. It is common in the literature to specify $\bar{f}_{R0}$, the background value of the field today ($a = 1$), rather than $\frac{c_1}{c_2^2}$. Smaller background field values lead to more screening of the fifth force and a smaller deviation from GR. In this work, we consider a $f(R)$ gravity model with a background field value of 10^{-5}. We refer to the scenario as "F5."

To consider perturbations, we assume a spatially flat, Friedmann-Robertson-Walker metric using the Newtonian gauge with Φ and Ψ denoting the gravitational potential and spatial curvature perturbations, respectively:

$$g_{\mu\nu}dx^\mu dx^\nu = a^2(\tau)[-(1+2\Phi)d\tau^2 + (1-2\Psi)\gamma_{ij}dx^i dx^j], \quad (6)$$

where τ is the conformal time, a is the scale factor set to $a = 1$ today and γ_{ij} is the 3D metric on spatial slices of constant τ.

In GR, the gravitational potential appearing in the metric which determines geodesics in the low-energy limit is the Newtonian potential $\Phi = \Phi_N$, which obeys the subhorizon Poisson equation

$$\nabla^2\Phi_N = 4\pi G a^2\delta\rho, \quad (7)$$

where $\delta\rho = \rho - \bar{\rho}$, the deviation of the cold dark matter density from its mean background value. In $f(R)$ gravity, the new scalar field f_R acts to source a fifth force through modifications to Φ so that instead of the total Φ satisfying (7), we have

$$\Phi = \Phi_N - \frac{1}{2} f_R, \tag{8}$$

where Φ_N still satisfies (7) but the new scalar field f_R satisfies a nonlinear field equation given by

$$\nabla^2 f_R = \frac{1}{3} a^2 \delta R(f_R) - \frac{8}{3} a^2 \pi G \delta\rho, \tag{9}$$

where $\delta R(f_R) = R(f_R) - \bar{R}$, and $R(f_R)$ is solved for by inverting (4).

In $f(R)$ gravity, the chameleon mechanism is responsible for increasing the mass of the scalar f_R in regions of high density thereby limiting its propagation. The flip side is that in regions of low density, this suppression shuts off and one may linearize the field equation for f_R in order to gain intuition for the fifth forces in void environments. Defining $\delta f_R = f_R - \bar{f}_R$ and linearizing (9) gives

$$\nabla^2 f_R = a^2 \mu^2 \delta f_R - \frac{8}{3} \pi G a^2 \delta\rho. \tag{10}$$

Solving this equation for a δ-function source yields the Yukawa potential, which features exponential suppression of f_R far from the source. Thus, while the ratio of coupling constants says gravity is enhanced by at most $1/3$ in $f(R)$ over its GR value, we should expect the fifth force in $f(R)$ gravity to be short ranged relative to the Newtonian force.

2. Dvali-Gabadadze-Porrati (nDGP) gravity

nDGP gravity [15] assumes our 4D Universe is confined to a 4D brane in a larger 5D spacetime with an action that includes both a 4D and a 5D term:

$$S_{\mathrm{nDGP}} = \int d^4x \sqrt{-g} \left(\frac{1}{16\pi G} R + \mathcal{L}_m(\psi_i) \right) + \int d^5x \sqrt{-g^{(5)}} \frac{1}{16\pi G} R^{(5)}. \tag{11}$$

The first integral contains both the standard Einstein Hilbert 4D action as well as the matter fields, constrained to live on the 4D brane, while the second integral is the 5D Einstein Hilbert action. $g_{\mu\nu}$ is the induced 4D metric on the 4D brane consistent with the total 5D metric $g^{(5)}_{AB}$.

Varying the action with respect the full 5D metric yields the 5D modified Einstein equations, while applying the Israel junction conditions across the 4D brane gives rise to the standard 4D Einstein equations on the braneworld plus a modification coming from the 5D bulk. A detailed analysis can be found in [92].

On the brane, the 4D induced metric still takes the form (3), meaning in the low-energy limit, particle geodesics are still determined by Φ, where we now have

$$\Phi = \Phi_N + \frac{1}{2} \varphi \tag{12}$$

with φ the "brane bending mode" referred to in [92] and Φ_N the standard Newtonian potential obeying (7). As can be seen from (12), the fifth force is now sourced by φ, which obeys the nonlinear field equation

$$\nabla^2 \varphi + \frac{r_c^2}{3\beta a^2} [(\nabla^2\varphi)^2 - (\nabla^i \nabla^j \varphi)(\nabla_i \nabla_j \varphi)] = \frac{8\pi G a^2}{3\beta} \delta\rho. \tag{13}$$

Here, r_c is the crossover scale, defined by the ratio of the 5D and 4D Newton constants [92]

$$r_c = \frac{1}{2} \frac{G^{(5)}}{G}, \tag{14}$$

and β is a time-dependent function given explicitly by [93]

$$\beta = 1 + H_0 r_c \frac{\Omega_{m0} a^{-3} + 2\Omega_{\Lambda 0}}{\sqrt{\Omega_{m0} a^{-3} + \Omega_{\Lambda 0}}}. \tag{15}$$

The screening mechanism employed by nDGP gravity is the Vainshtein mechanism. That this mechanism causes suppression to the additional scalar degree of freedom scalar wherever its derivatives become large can be seen explicitly in (13), in which the term in the square brackets, responsible for the screening, depends not on the value of φ but on its derivatives. This is in contrast to the chameleon mechanism in $f(R)$ gravity which depends on the value of the additional scalar f_R itself.

Within the literature, different models of nDGP gravity are specified by the value of $r_c H_0$. Larger values of r_c mean a stronger coupling to the screening term in square brackets and a smaller coupling to matter in (13). Hence, larger values of $r_c H_0$ lead to weaker modifications to gravity. In this work we consider the parameter value $r_c H_0 = 1$, which we refers to as "N1," consistent with other work in the literature.

Similar to our study of $f(R)$ gravity, we may linearize the nDGP field equation to gain intuition about the behavior of the fifth force in void environments. Linearizing (13) gives us

$$\nabla^2 \varphi = \frac{8\pi G a^2}{3\beta} \delta\rho. \tag{16}$$

The term in square brackets in (13) has been dropped as it is $\mathcal{O}(\varphi^2)$. At linear level, the fifth force in nDGP gravity features no additional screening and thus should have long-range solutions comparable to the Newtonian force within void environments. Comparing the matter coupling constants in (16) and (7) along with the extra factor of $1/2$

in (12), with $H_0 r_c = 1$, $\Omega_M \sim 0.3$, and $\Omega_\Lambda \sim 0.7$, gravity is increased by approximately 12% in nDGP gravity when in the linear regime.

B. Modified gravity simulations and HODs

In this paper we use the MG-GLAM simulations described in [94–96] to investigate nDGP and $f(R)$ gravity scenarios in comparison with a ΛCDM baseline. MG-GLAM is a particle-mesh code created to quickly simulate fully nonlinear N-body simulations of modified gravity. MG-GLAM uses a multigrid relaxation technique to solve the nonlinear field equations of these models, (9) and (13) for $f(R)$ and nDGP gravity, respectively.

The simulations consist of 100 realizations each for baseline GR with a ΛCDM cosmology, nDGP gravity with $H_0 r_c = 1$ (N1), and $f(R)$ gravity with $|\bar{f}_R| = 10^{-5}$ (F5). The cosmological parameters are also the same as those described in [95] and are chosen to match the 2015 Planck cosmological parameters [97]. Explicitly, $\Omega_m = 0.3089$, $h = 0.6774$, $n_s = 0.9667$, and $\sigma_8 = 0.8159$. The exact simulations used in this paper are larger than those presented in [95], although with the same mass and force resolutions. Each realization evolves 2048^3 particles of identical mass $1.1 \times 10^{10} M_{\rm sun}/h$ in a periodic box of comoving size $L_{\rm box} = 1024$ Mpc/h, initialized at a redshift of $z_{\rm initial} = 100$ with initial conditions generated using the Zel'dovich approximation [98]. All of our analysis is performed using the $z = 0.5$ snapshot.

Particles are grouped into halos using the bound density maxima halo finder described in [99]. Each halo catalog is complete down to a minimum halo mass of $M_{\rm Min} \simeq 10^{12.5} M_{\rm sun}/h$, which is taken as the minimum halo mass for all analysis involving dark matter halos [100].

While different modified gravity models will change the growth of dark matter large-scale structure, as captured in the halo one-point and two-point functions [101,102], it is the galaxies within dark matter halos, not the dark matter itself, that are observable. In order to get results which can be indicative of the statistics measured observationally with a galaxy survey, we must first augment the halo catalog with an appropriately tuned halo occupation distribution (HOD) function to model how a realistic galaxy population is assigned to the halos [103,104]. A HOD must be tuned to the simulations of each gravity theory separately so that the two-point galaxy correlation function matches that of a given, target observational dataset. We implement the HOD prescription laid out in [105], which is explicitly given by

$$\langle N_{\rm cen}(M)\rangle = \frac{1}{2}\left[1 + {\rm erf}\left(\frac{\log M - \log M_{\rm min}}{\sigma_{\log M}}\right)\right], \quad (17)$$

$$\langle N_{\rm sat}(M)\rangle = \langle N_{\rm cen}\rangle \left(\frac{M - M_0}{M_1}\right)^{\alpha}, \quad (18)$$

where $\langle N_{\rm cen}(M)\rangle$ and $\langle N_{\rm sat}(M)\rangle$ are, respectively, the number of central galaxies and satellite galaxies a halo of mass M will hold on average. The model parameters are obtained by fitting to the simulation's two-point function against observational survey data. Here, parameter values for $[M_{\rm Min}, M_0, M_1, \sigma_{\log M}, \alpha]$ for GR, F5, and N1 are taken from Table II in [106], with the GR parameter values representing the best fits to the BOSS CMASS DR9 dataset [107] and modified gravity parameters tuned to match the resulting GR projected galaxy two-point correlation function.

We compute the probability that a given halo of mass M hosts a galaxy as

$$\langle N_{\rm tot}(M)\rangle = \langle N_{\rm cen}(M)\rangle + \langle N_{\rm sat}(M)\rangle. \quad (19)$$

If $\langle N_{\rm tot}(M)\rangle \geq 1$, that halo is assumed to have at least one galaxy with certainty. If $\langle N_{\rm tot}(M)\rangle < 1$, we assign a galaxy with probability $\langle N_{\rm tot}(M)\rangle$.

C. Void finding procedure

We identify voids using the two different populations of tracers: the full set of halos and the subset of halos containing an HOD-identified mock galaxy.

Voids are identified in real space using the void finding package VIDE (void identification and examination toolkit) [108]. VIDE implements ZOBOV (zones bordering on voidness) [109] which uses a Voronoi tessellation followed by a watershed algorithm to divide all of space into cells around each tracer and then merge neighboring cells into "zones" to identify depressions in the local matter density. All zones are identified as individual voids, with no additional merging of zones. For VIDE users, this means we select all "bottom-level" voids, excluding all *parent* voids which are formed by joining regions with multiple *child* voids. This approach avoids overlaps within our void population and facilitates a more direct comparison with Ref. [33].

VIDE assigns each void an effective radius $R_{\rm eff}$ such that a sphere of radius $R_{\rm eff} = (3V_{\rm void}/4\pi)^{1/3}$ would have equal comoving volume $V_{\rm void}$ to the void in question (which may not be spherical in itself).

Each void's location is specified by its *circumcenter*, defined as the center of the largest sphere entirely empty of tracers which can be circumscribed inside the void in real space [110]. Note this is different from the void *macrocenter*, which is the VIDE default and defined as the volume weighted average position of all tracers within the void [108]. As shown in [111] (Appendix A), void circumcenters have been found to have a higher correlation with the maxima of the void gravitational potential than the macrocenters.

Note that the circumcenter of each void is empty of biased tracers by definition. This means that, consequently, we do not impose the optional central density threshold for

void identification within VIDE (typically requiring that a void must have a central density less than $0.2\bar{n}_{\rm sim}$).

D. Void stacking and multipole moments

Although any particular void located in real space is not perfectly spherical, the lack of a preferred axis means that when many voids are averaged or stacked together, the resulting matter distribution will be highly spherically symmetric. When computed numerically, the average density contrast for stacked voids in real space is given by

$$\delta^r(r) = \frac{N_h(r)}{N_v \bar{n}_h V(r)} - 1. \tag{20}$$

The superscript r denotes real space, n_h is the average number density of tracers (either of all halos or the subset of halos containing mock galaxies), $V(r)$ is the volume of the spherical shell ranging from $r - dr$ to $r + dr$, $N_h(r)$ is the total number of tracers in the shell, and N_v is the total number of voids in the stack.

In redshift space, spherical symmetry is no longer maintained. Using the distant observer approximation, tracer positions will shift from real space to redshift space according to

$$\mathbf{s} = \mathbf{r} + \frac{\mathbf{v}\cdot\hat{\mathbf{l}}}{\mathcal{H}}\hat{\mathbf{l}}, \tag{21}$$

where $\mathbf{v}$ is the tracer velocity, $\hat{\mathbf{l}}$ is the line of sight direction, commonly taken as $\hat{\mathbf{x}}$, $\hat{\mathbf{y}}$, or $\hat{\mathbf{z}}$, $\mathbf{s}$ is the position in redshift space, $\mathbf{r}$ is the position in real space, and $\mathcal{H} = d\ln a/d\tau = aH(a)$ is the conformal time Hubble factor.

The density contrast for stacked voids in redshift space is computed numerically using

$$\delta^s(s,\mu_s) = \frac{N_h(s,\mu_s)}{N_v \bar{n}_h V(s,\mu_s)} - 1, \tag{22}$$

where tracers are now binned using both a radial coordinate relative to their void center, s, and angular coordinate relative to the line of sight (LOS), $\mu_s = \cos(\theta_{LOS})$. The superscript "$s$" is used to denote the redshift space quantity. In both real space and redshift space, we use 50 equally separated radial bins of width $\Delta r = \Delta s = 2.4\,\mathrm{Mpc/h}$, and in redshift space, 100 equally separated angular bins for $\mu_s = \cos(\theta_{\rm LOS})$ ranging from $[-1, 1]$. $N_h(s,\mu_s)$, and $V(s,\mu_s)$ are defined similarly to their real space counterparts now with the inclusion of angular dependence.

The void-galaxy multipole moments $\xi_\ell(s)$ for $\delta^s(s,\mu_s)$ are defined as

$$\xi_\ell(s) = \frac{2\ell+1}{2}\int_{-1}^{1} \delta^s(s,\mu_s) P_\ell(\mu_s) d\mu_s, \tag{23}$$

where P_ℓ is the ℓth Legendre polynomial. In this analysis, we focus our attention on the void quadrupole ξ_2, the first nonzero redshift space multipole moment induced entirely by the effects of redshift space distortions. In this theoretical analysis we consider the average ξ_2 signal over all 100 realizations and three independent line of sight directions.

We note that the commonality of void density profiles under a rescaling by each void's effective radius $\tilde{r} \equiv r/R_{\rm eff}$ has been used in the literature to motivate stacking voids using the "rescaled" coordinate $\tilde{r}$ [64,112]. In the main text of this paper, we present results for voids stacked without such a rescaling; however, in the Appendix, we also provide the accompanying results for voids stacked using rescaled coordinates.

E. Gaussian streaming model

We employ the Gaussian streaming model (GSM) [113,114] to model the redshift space void quadrupole moment from the simulated real space data.

The coordinate change from real to redshift space coordinates, r and s, respectively, for transverse ($\perp$) and line of sight ($\parallel$) directions are given by

$$\begin{aligned} s_\perp &= r_\perp, \\ s_\parallel &= r_\parallel + \frac{v_r(r)\mu_r}{\mathcal{H}} + \frac{v_\parallel}{\mathcal{H}}. \end{aligned} \tag{24}$$

Here $r = \sqrt{r_\perp^2 + r_\parallel^2}$, $\mu_r = r_\parallel/r$, v_r is the coherent radial velocity flow in real space and $v_\parallel$ models random line of sight deviations around the coherent radial velocity.

The probability density function for $v_\parallel$, $\mathcal{P}$, is taken as a zero-mean Gaussian wholly specified by the dispersion in the line of sight velocity, $\sigma_{v_\parallel}(r,\mu_r)$, which has both radial and angular dependence. In practice, however, we find that the angular dependence is extremely weak compared to the radial dependence, with $\sigma_{v_\parallel}(r,\mu_r)$ an increasing function of μ_r but with $\sigma_{v_\parallel}(r,\mu_r=1)$ only greater than $\sigma_{v_\parallel}(r,\mu_r=0)$ by on average $\sim$1% when considering above median size voids in GR. Because of this, we neglect the angular dependence in $\sigma_{v_\parallel}$ and use $\sigma_{v_\parallel}(r) \simeq \sigma_{v_\parallel}(r,\mu_r=1) \equiv \sigma_{v_r}(r)$ to quantify $\sigma_{v_\parallel}$ from the simulations in the remainder of this work. We find that this approximation does not change any of the results presented.

Explicitly, this means the probability density function for $v_\parallel$ is given by

$$\mathcal{P}(v_\parallel) = \frac{1}{\sqrt{2\pi}\sigma_{v_\parallel}(r)} \exp\left(-\frac{v_\parallel^2}{2\sigma_{v_\parallel}(r)^2}\right), \tag{25}$$

where the distribution $\mathcal{P}$ is always implicitly a function of r. The GSM allows us to write the redshift space density distribution in terms of the real space quantities as

$$1+\delta^s(s,\mu_s)=\mathcal{H}\int dr_\parallel(1+\delta^r(r))\mathcal{P}(v_\parallel(r_\parallel,s,\mu_s)), \quad (26)$$

where, using (24), $v_\parallel$ is given by

$$v_\parallel=(s_\parallel-r_\parallel)\mathcal{H}-\mu_r v_r(r). \quad (27)$$

We note that (26) is equivalent to the expression used in [33] (prior to expansion), where $v_\parallel$ is directly integrated over through the inclusion of the Jacobian from (27). This is also consistent with integrating over a (nonzero mean) velocity variable $v_\parallel \to v_\parallel + v_r\mu_r$ as in [31,115].

III. RESULTS

In this section, results related to the impact of the HOD on the void size function are discussed in Sec. III A. The dynamical properties of the HOD-identified void populations are described in Sec. III B. Section III C presents the redshift space quadrupole results across each theory of gravity.

A. Void size function

While halos provide a useful mechanism for studying dark matter properties, we also need to consider how surveys will sample the halos with the galaxy tracers they observe. We connect the two by considering a HOD that assigns mock galaxy tracers to dark matter halos in such a way as to reproduce a target (would-be observed) two-point galaxy correlation function, as described in Sec. II B.

In this section we compare the void count statistics for voids identified from halos and HOD derived mock galaxies in GR and the modified gravity models. We then assess how the imposition of a HOD modifies the predicted size and number density of identified voids, which will be important for the subsequent analysis.

The total void population counts and average sizes are summarized in Table I for both halo and HOD-identified voids. When halos, rather than HOD mock galaxies, are used we have more voids with a smaller median size and larger differences between each theory of gravity. When voids are identified using HOD mock galaxies, the number of voids decreases by ∼60%, while the median size of the void populations increases by about 40%. The results in Table I show how using HOD mock galaxies as tracers eliminates differences in the median void size across theories of gravity and brings the total number of voids per realization back into agreement across all three theories.

Figure 1 provides more detail by showing the effect that tracer selection in the void identification process has on the resulting void size function (VSF), which we define as the number density of voids as a function of their effective radius.

Relative to the statistical uncertainties, the void size function for voids identified from halos can clearly distinguish between GR and F5 but not between N1 and GR. In $f(R)$ theories structure growth is enhanced relative to GR, leading to a larger number of halos above the minimum mass cutoff. The total number of voids identified with VIDE (or essentially any other void finder) is heavily dependent on the number density of tracers used to identify voids, as higher densities enable the identification of smaller voids [116,117]. Given a set of tracers on which a watershed algorithm has been run, adding additional tracers can only ever increase, or leave unchanged, the number of catchment basins identified. As such, the relative increase of 13% in the number of voids identified in F5 relative to GR follows naturally from the 12% increase in the number of halos in the F5 simulations. N1, by contrast, has a 2% fractional increase in number of halos relative to GR, and this gives rise to a 1% increase in the number of voids, indistinguishable from GR when considered relative to the estimated errors.

When we switch from halos as tracers to HOD-populated mock galaxies, Fig. 1 shows that the differences between GR and F5 disappear; the VSF for GR, N1 and F5 generally aligns well within the statistical uncertainties for the GR sample. This dramatic change in the HOD-derived void number function relative to that derived from halos highlights the need to take care in the void identification process.

B. Void density and velocity properties

Given that the void size function is equalized between GR and both N1 and F5 when voids are identified using HOD mock galaxies as opposed to halos, it is natural to ask how other void properties might be affected in each modified gravity model relative to their GR values. Due

TABLE I. Comparison of the mean number of voids per realization, and their median effective radius $R_{\rm eff}$, for voids identified using halos [left] and HOD mock galaxies [right] as tracers, for each of the GR, F5 and N1 models. The 1σ statistical variations in the average values in one realization are also given.

	Halo-identified		HOD-identified	
Model	Number of voids	Median $R_{\rm eff}$ (Mpc/h)	Number of voids	Median $R_{\rm eff}$ (Mpc/h)
GR	9034 ± 76	24.7 ± 0.1	3811 ± 50	34.9 ± 0.2
F5	$10\,206 \pm 74$	23.7 ± 0.1	3775 ± 46	35.0 ± 0.2
N1	9118 ± 73	24.6 ± 0.1	3776 ± 52	35.0 ± 0.2

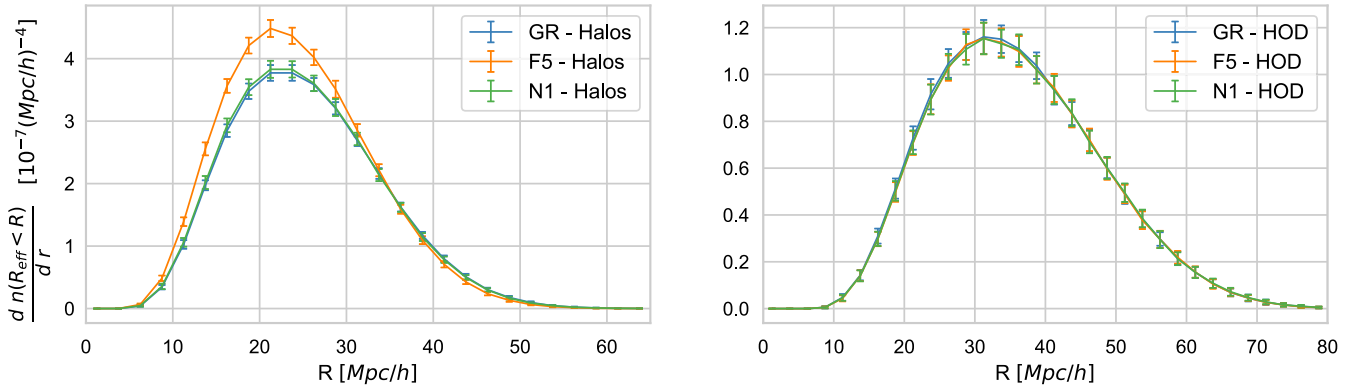

FIG. 1. The average void size function at $z = 0.5$ for GR [blue] and $f(R)$ F5 [orange] and nDGP N1 [green] in each model. Left: Voids are identified using halos with a minimum mass $10^{12.5} M_{\rm sun}/h$. Right: Voids are identified using a HOD tuned to ensure consistency in the galaxy two-point correlation function. Error bars represent statistical uncertainties on one realization.

to the differences in the fifth-force screening mechanism between each modified gravity theory [chameleon in $f(R)$, Vainshtein for nDGP], the application of an HOD has the potential to effect void properties in F5 and N1 in distinctly different ways.

Figure 2 shows the effects of the modifications to gravity, as well as the effects of tracer selection in the void identification process (halo or mock galaxy), on the radial velocity and velocity dispersion as a function of void size.

The ratio of the peak radial velocities, $v_{r,\rm peak,MG}/v_{r,\rm peak,GR}$, between F5 or N1 with respect to the GR value demonstrate the scale-dependent nature of each of the respective screening mechanisms. As shown in Ref. [78], the screening mechanism in $f(R)$ gravity is size dependent, and the magnitude of the fifth force to that of the Newtonian force for similarly shaped void density profiles is a decreasing function of $R_{\rm eff}$. By contrast, when linearized, the field equation for the fifth force in N1 (16) shows no scale dependence. Accordingly, the peak velocity ratio $v_{r,\rm peak,N1}/v_{r,\rm peak,GR}$ is much more constant with respect to $R_{\rm eff}$ compared to the F5 case.

The use of an HOD also dampens the F5 radial velocity profiles to a much larger degree than for N1. The screening mechanism in $f(R)$ gravity is known to be environmentally dependent [101,118], whereas the use of an HOD preferentially selects more massive halos to receive a mock galaxy and thus be used as tracers. Hence, we attribute the reduction in $v_{r,\rm peak,F5}/v_{r,\rm peak,GR}$ in the HOD selected sample relative to the halo selected one, seen in Fig. 2, to the preferential selection of more massive (and therefore more screened) halos, where the effect of the fifth force is reduced in F5.

The effect of the HOD on the N1 velocities is much less pronounced and provides neither a consistent increase nor decrease to $v_{r,\rm peak,N1}/v_{r,\rm peak,GR}$. In nDGP gravity, the nature of the Vainshtein screening mechanism is fundamentally different than that of the chameleon mechanism in $f(R)$ gravity. The Vainshtein mechanism heavily screens short-wavelength φ modes, such as those generated within halo environments, while leaving long-wavelength modes to remain mostly unscreened. For the N1 parameter value, almost all halos are already screened [101,119]—consistent

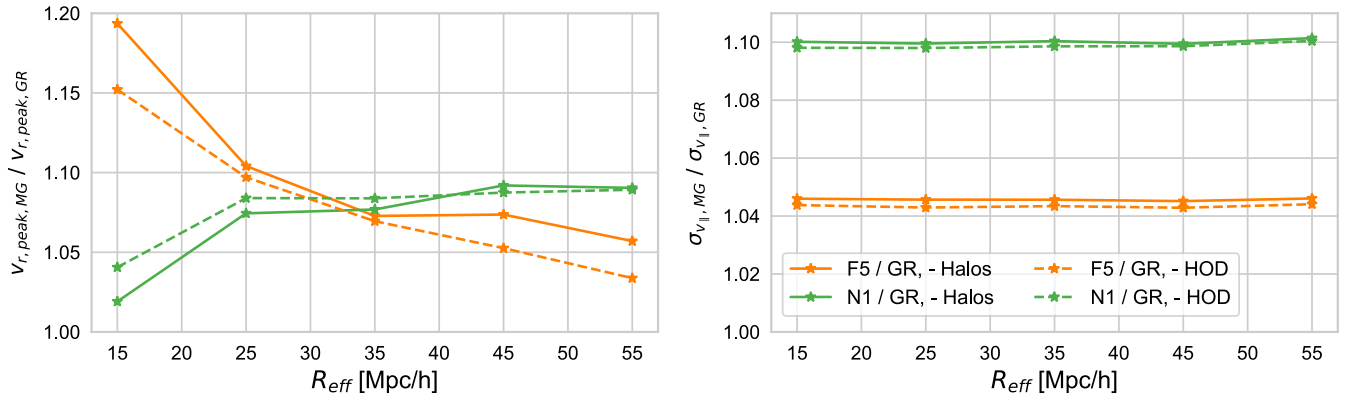

FIG. 2. Left: ratio of the peak radial velocity in F5 [orange] and N1 [green] to that in GR as a function of void effective radius $R_{\rm eff}$ for voids identified from halos [solid] and from halos containing mock galaxies identified by the HOD [dashed]. Right: ratio of the average asymptotic value of the velocity dispersion, at $r \gtrsim 40$ Mpc/h, as a function of $R_{\rm eff}$.

with the previously mentioned modest 2% fractional increase in the number of halos in N1 over GR. This means that the preferential selection of more massive halos through an HOD provides no additional suppression to the N1 velocities. Despite all halos in N1 appearing as screened, the derivative shift symmetry present in (13), $\partial_\nu\varphi \to \partial_\nu\varphi + c_\nu$, enables long-wavelength φ modes from distant sources in superposition with the φ profile sourced by a screened halo to together solve (13). This in turn allows these screened halos to move in response to the long-wavelength φ modes as if they were unscreened point particles, which allows for increases to v_r in N1 despite each tracer being screened [120]. This is also what allows the use of the linearized field (16) within void environments, as all relevant φ modes are long wavelength, sourced by the void environment itself or from distant halos.

Figure 2 also shows the relative change to the asymptotic value of $\sigma_{v_\parallel,N1}$ or $\sigma_{v_\parallel,\mathrm{F5}}$ with respect to the GR value as a function of void size. In both N1 or F5, and using either halos or mock galaxies to identify voids, there is no scale dependence in this value.

The greater velocity dispersion in modified gravity scenarios relative to GR is well documented (e.g., [121]) and can be traced back to the action of the fifth force increasing peculiar velocities. While the void environment is the driving factor in determining the average v_r, the same is not true of the velocity dispersion. Immediately outside the void, regardless of void size, we find that $\sigma_{v_\parallel}$ returns to its background value across the simulation as a whole, indicating that void environments themselves do little to determine the asymptotic value of $\sigma_{v_\parallel}$.

Given the scale-dependent nature of v_r in each modified gravity theory, it is informative to investigate behavior in two groups distinguished by size. We break the sample into two populations of smaller and larger voids, respectively, of sizes below and above the median size, $R_{\mathrm{eff}} = 35$ Mpc/h.

The top row of Fig. 3 shows the real space density profile δ^r, the void radial velocity profile v_r, and the velocity dispersion profile $\sigma_{v_\parallel}$ for the large and small void populations, for mock galaxy identified voids in GR, while the bottom row displays the change in each of these quantities in F5 or N1 over the respective GR value. In order to align most closely with, and inform, potential observation, all quantities in Fig. 3 are calculated using the population of mock galaxies as tracers, and not the underlying halo population or dark matter particles. We note that, taken together, Figs. 2 and 3 are consistent with Figs. 9–11 in Ref. [122], who perform a similar analysis of voids in modified gravity with a different set of simulations.

From the point of view of theses biased tracers, the interiors of the voids are extremely rare with $1 + \delta_r \approx 0$. At the void edge, the density rapidly increases, with a mild overdensity at the void edge, which is more pronounced in small voids than large. The modified gravity models do not significantly change the density profile.

The radial velocity v_r is an increasing function inside the void interior before reaching its peak value just around the void edge, where the density contrast increases rapidly. The radial velocity from the large void sample is constantly larger in magnitude than that of the small voids, in accordance with linear theory. We find that both F5 and N1 increase the size of the velocity peak relative to GR, with both providing comparable increases in the small void population but N1 providing a larger and more spatially extended increase within the large voids.

The relative effects of the modified models can be understood through the linearized field equations. For

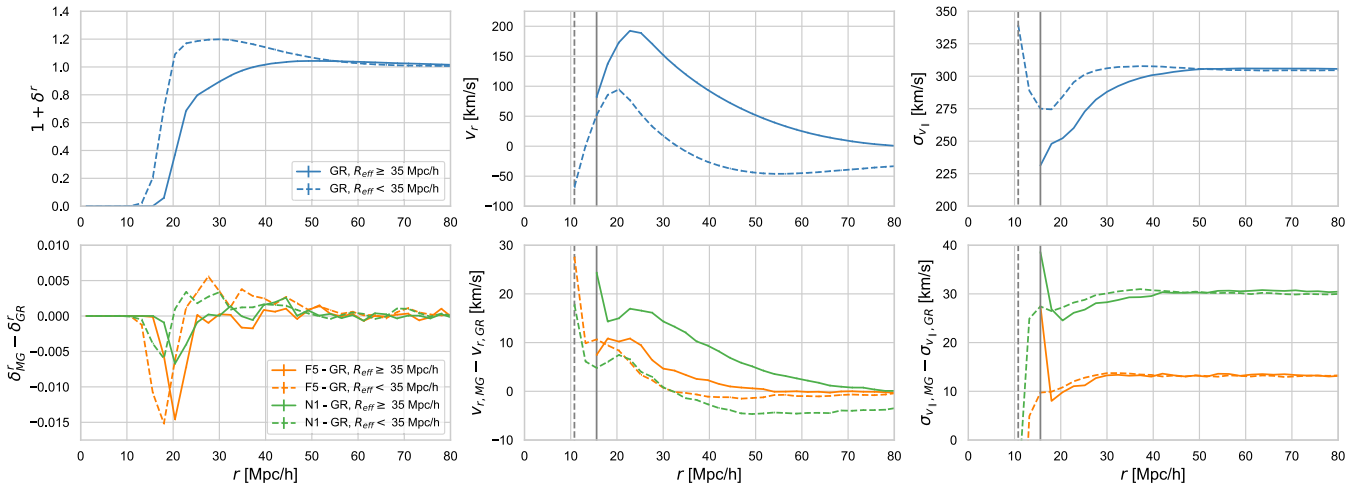

FIG. 3. Top row: void density [left], radial velocity [center] and velocity dispersion [right] profiles in GR for voids identified in halos with HOD-identified tracers. The void population is split into those with void size above [solid] and below [dashed] $R_{\mathrm{eff}} = 35$ Mpc/h, the median void size found in each of the three theories. Gray lines indicate the first radial bin below which no tracers are found. Bottom row: differences between F5 [orange] and N1 [green] quantities with respect to those in GR.

the $f(R)$ field (10) yields the Yukawa potential, and the resulting fifth force is short ranged in comparison with Newtonian gravity. In contrast, the linearized N1 field equation (16) features no screening term and is thus longer ranged than its F5 counterpart. This leads to a modification to the radial velocity profile Δv_r, which remains nonzero in N1 gravity over a much larger spatial extent compared to F5. This phenomenon can be seen in Fig. 3 for both small and large void populations alike. The $R_{\rm eff}$-dependent enhancement to v_r seen in Fig. 2 can also be seen in Fig. 3 by comparing the various curves in the bottom middle panel to those in the upper middle panel. In F5, the value of $\Delta v_r/v_{r,\rm GR}$ is largest in the small void population, while this quantity is much more similar in both void populations for N1.

While the qualitative changes to the radial velocities are quite distinct, the changes to the velocity dispersion induced by the modified gravity models are similar in F5 and N1. While Δv_r is largest within the void interior and the exact shape is sensitive to the intricacies of the particular model, increases in $\Delta\sigma_{v_\parallel}$ relative to GR are largely independent of the distance from the void, with $\sigma_{v_\parallel}$ tending toward a value determined by the large-scale properties of the simulated density field rather than the void itself.

In Fig. 3, $(1+\delta^r)$ is at most ∼1% different between GR and either modified theory in both void populations shown while peak values of v_r are increased at roughly the 5%–10% level over the GR values depending on the void population and theory of gravity considered. In the large void population, $v_{r,\rm peak}$ is increased by 9% in N1 and 6% in F5, while in the small void population, these numbers change to 8% in N1 and 9% in F5, respectively. For $\sigma_{v_\parallel}$, the asymptotic values increase by 10% in N1 and 4% in F5 independent of void population. In the following section we discuss the implications of these differences on the void quadrupole statistic.

C. Void quadrupole moments

In real space, stacked voids are spherically symmetric, and therefore the only nonzero multipole moment will be the monopole ξ_0, equal to the real space density contrast $\delta^r(r)$. For stacked voids in redshift space, Redshift Space Distortion(s) (RSD) effects under the distant observer approximation break this spherical symmetry along the line of sight, while preserving reflection symmetry across the plane which passes through the center of the void orthogonal to the LOS direction. The consequence of this reflection symmetry is that $\delta^s(s,\mu_s)=\delta^s(s,-\mu_s)$, which sets all redshift space ξ_ℓ with odd ℓ identically equal to 0. Thus, the quadrupole $\xi_2(s)$ is the first nonzero multipole moment induced entirely by redshift space distortions and will be the focus of the remainder of this work.

Given two of the three functions used by the GSM to predict $\delta^s(s,\mu_s)$ and ξ_2 see changes under modifications to gravity at roughly the 10% level, as discussed in the previous section, one might intuit a similar level of change

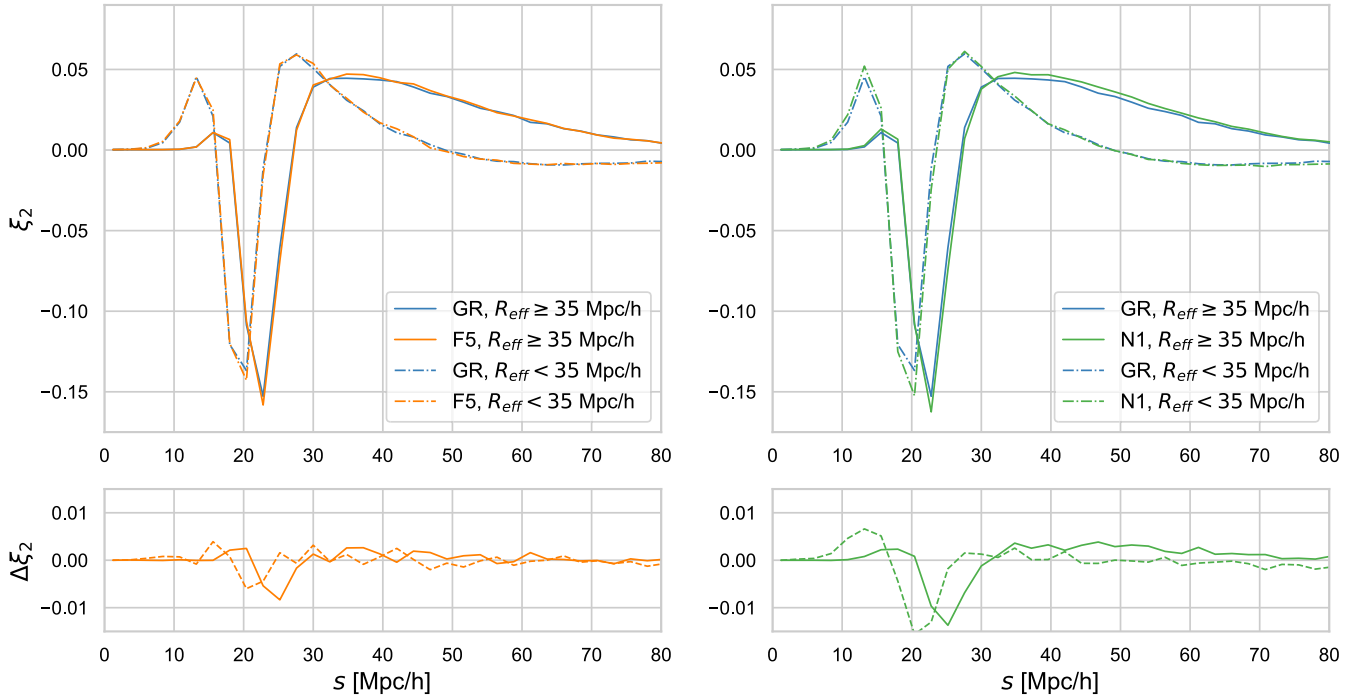

FIG. 4. Top row: the void quadrupole moment ξ_2 at $z=0.5$ for GR [blue] compared against F5 [left, orange] and N1 [right, green] in voids both below [dashed] and above [solid] the median void size. Bottom row: difference in ξ_2 between GR and each modified gravity theory in small [dashed] and large [solid] voids.

in ξ_2 for at least some of the void populations and modified gravity scenarios considered.

In Fig. 4 we present $\xi_2(s)$ for mock galaxy identified voids in GR, F5 and N1 in both the large and small void populations (defined with respect to the median void size, $R_{\mathrm{eff,median}} \simeq 35$ Mpc/h). Figure 4 is qualitatively consistent with the void quadrupoles shown in both Refs. [33,122].

For N1 gravity, given Fig. 2, we expect the largest deviation between $\xi_{2,N1}$ and $\xi_{2,\mathrm{GR}}$ to occur in large voids. Examining the population of larger voids, we find $\xi_{2,N1}$ is on average 8% larger than $\xi_{2,\mathrm{GR}}$ for $s \sim 35$–65 Mpc/h.

In the small void population, we see little to no difference between ξ_2 for N1 and GR, except for a very localized change in the minimum at the void edge.

Comparing F5 versus GR, we find $\xi_{2,\mathrm{F5}}$ and $\xi_{2,\mathrm{GR}}$ are strikingly similar in both the void populations except for some variation tightly located at the void edge. Although this might have been expected for the large voids, given the scale-dependent screening produces the largest $\Delta v_r/v_r$ in small voids (as in Fig. 2), the fact that there is little difference between $\xi_{2,\mathrm{F5}}$ and $\xi_{2,\mathrm{GR}}$ in the below median size void population does not follow that simple intuition.

IV. ANALYSIS

A. Gaussian streaming model predictions in modified gravity

We seek to understand why differences on the order 10% in the velocity variables v_r and $\sigma_{v_\parallel}$ (which both feature drastically different spatial profiles) do not induce comparable variations in ξ_2 between GR and the modified theories. To do this we employ the Gaussian streaming model which takes as inputs $\delta^r(r)$, $v_r(r)$, and $\sigma_{v_\parallel}(r)$ and returns a prediction for $\xi_2(s)$.

We first assess how well the GSM performs in each theory of gravity. Figure 5 compares the simulation-derived quadrupoles with the theoretical GSM predictions for N1 and F5 for both the large (above-median radius) and small (below-median) populations of voids identified with halos containing HOD-identified galaxies. Note that, to assess the accuracy and precision of the GSM prediction for each model, we compare the differences of the mean values relative to the errors on the mean signal from the full 100 realizations.

When taking the values of δ^r, v_r, and $\sigma_{v_\parallel}$ directly from the simulations, the GSM performs exceptionally well in all three gravity scenarios (GR not shown) and for both void size groups.

In both the small and large void population, at radial distances exceeding 15 Mpc/h, the GSM rarely exceeds statistical uncertainties in the mean estimated from the 100 realizations. As such, the GSM model is shown to provide a robust method with which to model the contributions to the quadrupole.

B. Dissecting the quadrupole

Given the GSM allows us to accurately model the quadrupole, we now use it to dissect and explain why

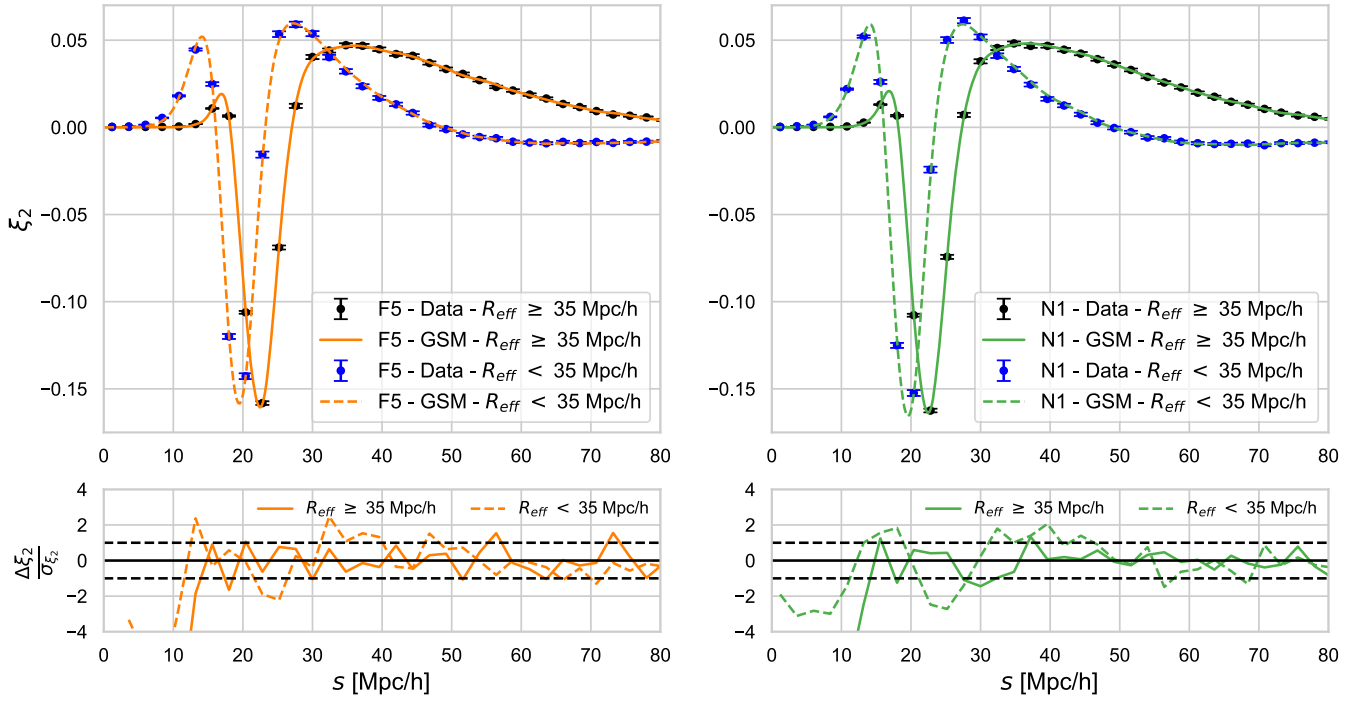

FIG. 5. Top: theoretical value of ξ_2 in voids both above [dashed] and below [solid] the median void size in F5 [left, orange] and N1 [right, green] calculated using the GSM compared to average ξ_2 from the simulations. Bottom: difference between the GSM-derived quadrupole and that from the simulated data, $\Delta\xi_2 = \xi_{2,\mathrm{GSM}} - \xi_{2,\mathrm{Data}}$, with respect to the statistical uncertainties for the model, σ_{ξ_2}.

the differences between ξ_2 in GR and modified gravity are so much smaller than the differences in the contributing v_r and $\sigma_{v_\parallel}$ might suggest.

As a mathematical object, the GSM is a functional, which we will denote with F. For each model of gravity, at a given redshift space radial coordinate s, it takes the three void density and velocity functions and returns the quadrupole $F(s, \delta^r, v_r, \sigma_{v_\parallel}) \to \xi_2(s)$. The functional picture of the GSM allows us to mix and match quantities from different gravitational scenarios to predict the hypothetical ξ_2. For example, we could compute $\mathrm{F}(s, \delta^r|_{\mathrm{GR}}, v_r|_{\mathrm{F5}}, \sigma_{v_\parallel}|_{\mathrm{GR}})$ in order to isolate the effect that F5's increased radial velocity has on ξ_2 while holding the density and velocity dispersion fixed at their GR values. These expressions, in turn, where one function takes on its F5 or N1 value and the others remain fixed at their GR values, can be calculated by taking the appropriate functional derivative of the GSM and integrating against the change in the corresponding quantity.

The total change in $\xi_{2,\mathrm{F5}}(s)$ or $\xi_{2,\mathrm{N1}}(s)$ relative to $\xi_{2,\mathrm{GR}}(s)$ can be approximated to a high degree of accuracy as the sum of the individual first-order changes to ξ_2 induced by the individual changes to δ^r, v_r, and $\sigma_{v_\parallel}$ in the modified gravity (MG) theories,

$$\xi_{2,\mathrm{MG}} - \xi_{2,\mathrm{GR}} \equiv \Delta\xi_2(s) = \Delta_{\delta^r}\xi_2 + \Delta_{v_r}\xi_2 + \Delta_{\sigma_{v_\parallel}}\xi_2, \quad (28)$$

where $\Delta_x\xi_2 \equiv (\mathrm{F}(x|_{\mathrm{MG}}, \ldots) - \mathrm{F}|_{\mathrm{GR}})$ for $x = \delta^r(r)$, $v_r(r)$, or $\sigma_{v_\parallel}(r)$. Each of the terms in (28) can be written as

$$\begin{aligned}\Delta_x\xi_2(s) &= \int dr \frac{\delta F}{\delta x}\Delta x \\ &= \frac{5}{4}\int_{-1}^{1} d\mu_s (3\mu_s^2 - 1)\Delta_x\delta^s(s, \mu_s). \end{aligned} \quad (29)$$

Here Δx indicates the difference in values of variable x between the MG and GR models and $\Delta_x\delta^s$ denotes the change induced in δ^s induced by the change in x. Suppressing the arguments of $v_\parallel(r_\parallel, s, \mu_s)$ for brevity, these functions are given by

$$\Delta_{\delta^r}\delta^s = \mathcal{H}\int dr_\parallel \mathcal{P}(v_\parallel)\Delta\delta^r(r), \quad (30)$$

$$\Delta_{v_r}\delta^s = \mathcal{H}\int dr_\parallel \frac{\mu_r v_\parallel}{\sigma_{v_\parallel}(r)^2}\mathcal{P}(v_\parallel)(1 + \delta^r(r))\Delta v_r(r), \quad (31)$$

$$\Delta_{\sigma_{v_\parallel}}\delta^s = \mathcal{H}\int \frac{dr_\parallel}{\sigma_{v_\parallel}(r)}\mathcal{P}(v_\parallel)\left(\frac{v_\parallel^2}{\sigma_{v_\parallel}(r)^2} - 1\right)(1 + \delta^r(r))\Delta\sigma_{v_\parallel}. \quad (32)$$

Figure 6 shows the changes induced in ξ_2 independently by changes to δ^r, v_r, and $\sigma_{v_\parallel}$, respectively, as calculated using the functional derivative approach and compares them to the total changes in ξ_2 from the simulations. The figures show results for the small void population in F5 and the large void population in N1 motivated by Fig. 2, in which it is small voids in F5 and large voids in N1 which would receive the greatest increases in their radial velocity profiles and therefore provide the most interesting case studies. The total $\Delta\xi_2$, as calculated from the simulation data directly, is shown to be accurately reproduced by the sum of the individual changes as calculated using the functional derivative approach described in (28). As a result, we use this approach to examine the individual terms to understand their respective roles in inducing changes to ξ_2 in the modified gravity scenarios.

To get an intuitive understanding of the individual changes shown in Fig. 6, we can consider the contributions from the line of sight, $\mu_s = \mu_r = \pm 1$. This is where the bulk of the contribution to both $\Delta_{v_r}\xi_2$ and $\Delta_{\sigma_{v_\parallel}}\xi_2$ is derived, which can be understood by noting that $\mu_s = \pm 1$ is where $P_2(\mu_s) \propto (3\mu_s^2 - 1)$ is maximized, and also where v_r may have the greatest impact on the real to redshift space coordinate change in accordance with (24).

Figure 6 shows that changes induced by Δv_r provide the dominant contribution to $\Delta\xi_2$ outside the void in both small F5 voids and large N1 voids. Physically, the positive increases induced by the MG models to the outflowing radial velocity v_r shift matter further away from the void under redshift space distortions. This causes a negative spike in $\Delta_{v_r}\delta^s(s, \mu_s = 1)$ [and therefore $\Delta_{v_r}\xi_2(s)$] closer to the void (where tracers streamed to without the increase) and a positive spike at larger s (where tracers stream to now).

The negative and positive peaks in $\Delta_{v_r}\xi_2(s)$ are roughly localized to the radial positions with coincident large positive $\Delta v_r(r)$ and nonzero $(1 + \delta^r)$. In F5, due to the short range of the fifth force, Δv_r is also short ranged and does not extend far beyond the void interior. Hence, $\Delta_{v_r}\xi_2(s)$ is also spatially limited to the void edge region when considering F5 modifications. In N1, the fifth force is longer ranged, and thus so is Δv_r—extending well beyond the void edge out to almost 80 Mpc/h as shown in Fig. 3. This causes $\Delta_{v_r}\xi_2(s)$ to decouple from the void edge region and to have a much longer spatial extent in the N1 voids considered, as can be seen in Fig. 6.

As shown in Fig. 3, in contrast to Δv_r, $\Delta\sigma_{v_\parallel}$ is a roughly constant function of r regardless of void size or model of gravity. In theory then one might expect this to induce changes in ξ_2 at all radii. Nevertheless, as shown in Fig. 6, the effects of changes to the velocity dispersion are principally focused around the void edge. To understand why the signal is suppressed at larger radii, we note that in this region $\delta^r(r)$, $v_r(r)$, and $\sigma_{v_\parallel}(r)$ are all effectively constant. In this limit, (32) can be simplified to read (using subscript 0 to denote variable constant values)

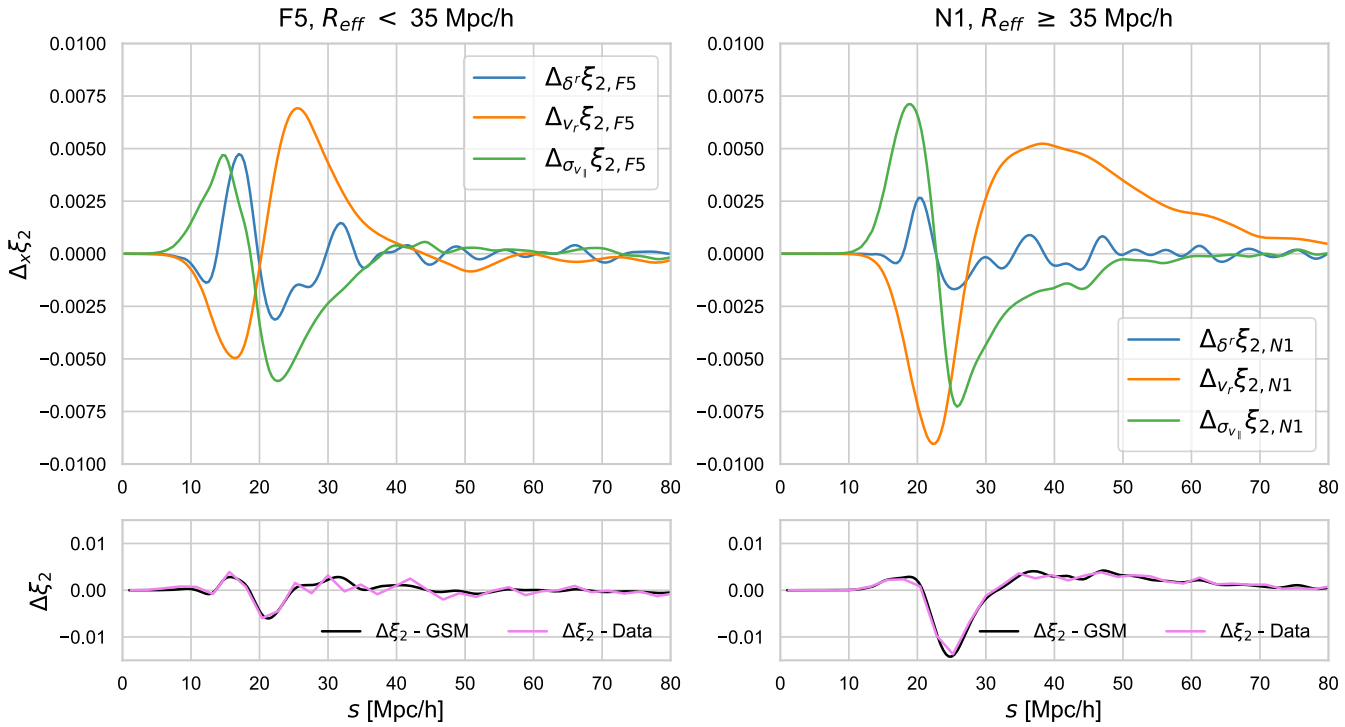

FIG. 6. Two scenarios are considered: [left] below median size voids in F5 and [right] above median size voids in N1. Top row: the changes to ξ_2 relative to GR induced independently by $\Delta\delta^r$ [blue], Δv_r [orange], and $\Delta\sigma_{v_\parallel}$ [green] as calculated using GSM functional derivatives. Bottom row: comparison of the differences, $\Delta\xi_2$, between the modified gravity model and GR obtained from the simulated data in F5 [left, violet] and N1 [right, violet] and the summed GSM integrated functional derivatives [black].

$$\Delta_{\sigma_{v_\parallel}}\delta^s \approx \frac{\mathcal{H}(1+\delta_0^r)(\Delta\sigma_{v_\parallel,0})}{\sqrt{2\pi}\sigma^2_{v_\parallel,0}}\exp\left(-\frac{v_\parallel^2}{2\sigma^2_{v_\parallel,0}}\right)v_\parallel\Big|_{-\infty}^{+\infty} = 0. \tag{33}$$

We therefore expect that $\Delta_{\sigma_{v_\parallel}}\xi_2(s)$ will be very close to zero except where at least one of $\delta^r(r)$, $v_r(r)$, $\sigma_{v_\parallel}(r)$, or $\Delta\sigma_{v_\parallel}$ is changing rapidly with radial position in the vicinity of the associated $r \sim s$. The functions with the biggest potential impact in this regard are $\Delta\sigma_{v_\parallel}$ and δ^r, as they both enter (32) as overall multiplicative factors. In Fig. 3, we find $\Delta\sigma_{v_\parallel}$ in both theories of gravity and both void populations is almost constant, while δ^r changes rapidly near the void edge. This in effect tethers the changes induced in ξ_2, by $\Delta\sigma_{v_\parallel}$ to this region, despite the fact that $\Delta\sigma_{v_\parallel}$ remains nonzero far outside of the void.

Examining this void edge region, increasing $\sigma_{v_\parallel}$ increases the amount of "shuffling" of matter between neighboring radial bins which occurs during the move from real to redshift space. Near the void edge, however, this shuffling is highly asymmetrical between the void interior and exterior. The void interior is mostly empty and, thus, has very little matter which can stream out. The void exterior, by contrast, has $(1+\delta^r) \sim 1$ and, thus, has some of its own matter shifted into the void while receiving almost none in return from the void center in the move from real to redshift space. This phenomena is again most pronounced along the line of sight, and increasing $\sigma_{v_\parallel}$ increases the severity. This means that $\Delta_{\sigma_{v_\parallel}}\delta^s$ will be positive for s values within the void interior, negative for those s values just outside of the void edge, and 0 for large s values, with $\Delta\sigma_{v_\parallel}\xi_2$ following the same phenomenology.

$\Delta\delta^r$ is small compared to $(1+\delta^r|_{\rm GR})$, as shown in Fig. 3. As such, $\Delta\delta^r$ plays only a minor role in determining the total $\Delta\xi_2$ through (30).

The discussion above outlines why increases in the radial velocity and velocity dispersion due to the modifications to gravity combine to give only minimal or no effect on ξ_2 in most instances. In summary, Δv_r and $\Delta\sigma_{v_\parallel}$ have opposing effects on ξ_2. Increases to v_r drive material outward while increases to $\sigma_{v_\parallel}$ lead to the net movement of material inward from the overdensity at the void edge. The end result is cancellation between $\Delta_{\sigma_{v_\parallel}}\xi_2$ and $\Delta_{v_r}\xi_2$, leading to the total $\Delta\xi_2$ being much smaller than the individual changes to v_r and $\sigma_{v_\parallel}$. An exception to this occurs in the large N1 voids at intermediate scales, ~35–65 Mpc/h. In N1, Δv_r is long ranged, which similarly extends the spatial range of $\Delta_{v_r}\xi_2$ and lessens its cancellation against $\Delta_{\sigma_{v_\parallel}}\xi_2$—yielding the observed $\Delta\xi_2/\Delta\xi_{2,\rm GR} \sim 8\%$ over this

range. In both F5 void populations, there is no significant difference from GR. The effects of the MG model are constrained to the void edge region where there is a direct cancellation, discussed above.

We have focused on the behavior of the quadrupole moment ξ_2 justified by noting that it is the first nonzero multipole moment induced entirely by redshift space distortions, as $\xi_0 = \delta^r$, $\xi_{\ell\geq 1} \equiv 0$ for stacked real space voids. We note that the functional derivative approach can be applied similarly to higher-order even moments by the appropriate substitution of the Legendre polynomials in (29) to isolate the effect of $\Delta\delta^r$, Δv_r, and $\Delta\sigma_{v_\parallel}$ on $\Delta\xi_0(s)$, $\xi_4(s)$, or any higher-order even multipole moment (all odd moments are still identically 0 by symmetry). We find that the impact of the modified gravity model on the hexadecapole, ξ_4, is much smaller than that for the quadrupole largely due the greater spatial oscillation in the higher-order Legendre polynomial. As such, ξ_2 provides the best-case scenario to test modified gravity with void multipole moments.

C. Fitting ξ_2 with the (β,σ_0) model

In this section we consider the application of the measured void quadrupole to constrain the underlying cosmological theory. We use the quadrupole to constrain the cosmological parameter $\beta = f/b$, where $f = d\ln\delta_{\rm DM}/d\ln a$ is the dark matter logarithmic growth rate and b is the galaxy tracer bias [33,40,90].

Within the context of GR and linear theory, the void radial velocity profile is given by

$$v_r(r) = -\frac{\beta}{3}\mathcal{H}\Delta(r)r, \tag{34}$$

where $\Delta(r)$ is the average density within a radius r,

$$\Delta(r) \equiv \frac{1}{\frac{4}{3}\pi r^3}\int_0^r 4\pi\delta^r(r')r'^2 dr'. \tag{35}$$

Here $\beta = f/b$ is employed instead of f since we calculate $\Delta(r)$ using the galaxy number density contrast δ^r instead of the underlying dark matter density contrast itself.

Before considering the constraints from ξ_2, we first consider how well a constant β is able to model the radial velocity profile. We can do this because the simulations provide complete knowledge of all tracer velocities and can explore the connection between β and v_r directly. We find that for the above median size voids the linear relationship in (34) holds very well. We find for the below-median size void population that (34) does not provide a good fit for the entirety of v_r. This is consistent with findings presented in Ref. [117], where v_r in the smaller void populations, similar to our sample, was found to be fit less well by linear theory compared to larger voids due to sparce tracer sampling.

TABLE II. Comparison of the constraints [left] on the (β,σ_0) model fit to the void quadrupole $\xi_2(s)$ in each theory of gravity and [right] with the purely theoretical value of β obtained from the void velocity profile, v_r, which is not a survey observable.

	Fit from ξ_2		Theory fit to v_r
Model	σ_0 (km/s)	β	β
GR	278 ± 17	0.36 ± 0.03	0.36 ± 0.003
F5	287 ± 18	0.37 ± 0.03	0.37 ± 0.003
N1	304 ± 18	0.39 ± 0.03	0.39 ± 0.003

In Table II, we show the best-fit values of β inferred from a fit of the average radial velocity, v_r, using (34) for the above-median size void population for each theory of gravity along with the uncertainty in β given the covariance in the mean v_r. Modifications to gravity increase v_r, which in the context of (34) lead to an increase in the inferred β.

While the simulations give us direct access to the velocity information, real world observational programs do not. However, we can still use the measured quadrupole moment ξ_2 along with the GSM to constrain the cosmological parameter β. We use a modified version of the GSM where only an average void density profile δ^r is assumed along with two cosmological parameters β and σ_0, which replace direct knowledge of both functions containing velocity information. An effective v_r is then constructed using β in conjunction with (35), while the velocity dispersion is set to a constant effective value $\sigma_{v_\parallel}(r) = \sigma_0$. This (β,σ_0) model is a simple parametrization used to capture the dynamics within void environments without having to have an exact knowledge of the two functions containing velocity information.

To determine the theoretical applicability of this approach, we consider the mean ξ_2 measured across the 100 simulations but estimate the signal covariance using the uncertainties from a jackknife from a single realization with volume of $\sim(1\ {\rm Gpc/h})^3$.

Figure 7 shows the best-fit values and the corresponding 68% confidence interval for β and σ_0 recovered from the joint 2D fit to ξ_2. The plot also shows the value of β recovered directly in each theory from fitting the average void v_r profile using (34). The 1D projected constraints on the (β,σ_0) fit parameters for the three gravity models are summarized in Table II.

The 1D value of β recovered by each method match, showing that the ξ_2 fit, including σ_0, does not bias the recovered value of β. The values of σ_0 do not match the asymptotic values of $\sigma_{v_\parallel}$ shown in Fig. 3. This is due to the fact that, as previously discussed, as long as $\sigma_{v_\parallel}$ is constant, ξ_2 is fairly insensitive to its exact value away from the void center. Thus, the value σ_0 takes is more sensitive to dynamics near the void edge and less to the actual asymptotic value of $\sigma_{v_\parallel}$. It is to be expected therefore that the value of σ_0 should be lower than the asymptotic value far from the void center. This is consistent with what

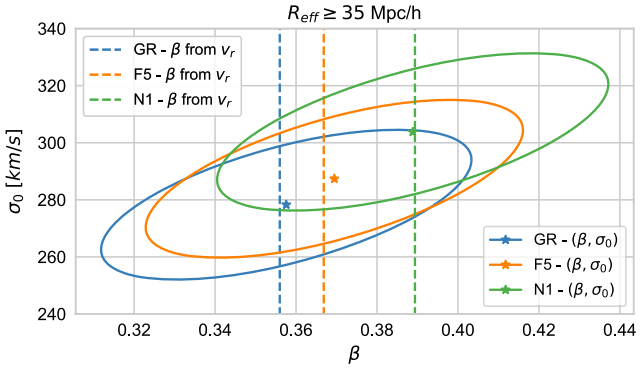

FIG. 7. The linear growth rate-dependent parameter, β, calculated from v_r directly using linear theory [dashed lines], compared with the best fit [star] and the 68% confidence ellipses [full line] from ξ_2 modeled using the GSM with the (β, σ_0) parametrization, in GR [blue], F5 [orange], and N1 [green]. The model is fit to the mean quadrupole from 100 realizations for the above-median size void sample with confidence ellipses derived from statistical uncertainties estimated for one realization, with volume $(1.024\ \mathrm{Gpc/h})^3$.

we find. For GR, for example, $\sigma_{v_\parallel}$ asymptotes to a value of 305 km/s while σ_0 is 278 km/s, while for F5 the values are 318 and 287 km/s, respectively.

In this analysis we jointly constrain β and σ_0 and assume our knowledge of the density comes from the observed galaxy tracers. We note recent work [122] considered monopole and quadrupole constraints on β in modified gravity models but assumed perfect knowledge of $\sigma_{v_\parallel}(r)$ and the underlying CDM density Δ.

While N1 and F5 have larger predicted values of β than GR, the values obtained for the three models are indistinguishable within the estimated uncertainties at the 68% confidence level considering the volume observable within this $z = 0.5$ redshift slice. This opens up the possibility, however, that combining data from multiple redshift slices (to increase the observational volume and lower the level of statistical uncertainties) could provide a way to increase sensitivity and allow the application of the void quadrupole to distinguish between models in this way.

V. CONCLUSIONS

In this paper we utilize the large-scale, high-precision N-body MG-GLAM simulations [94–96] of GR, $f(R)$, and nDGP gravity to compare real space dynamical properties of voids and the resulting redshift space quadrupole moments, as might be measured from upcoming spectroscopic galaxy survey such as from the DESI, Euclid and Roman experiments. This work builds on of our previous work [78], where scale-dependent effects were observed in void peculiar velocities within $f(R)$ gravity.

While the properties of voids can be investigated using dark matter halos as biased tracers of the underlying dark matter distribution itself, in order to compare with observations, we consider how the void statistics are modified by the inclusion of a HOD. We find that it is vital to include the effects of a HOD when identifying voids and calculating the resulting statistics. The application of a HOD significantly effects the void size function in the $f(R)$ model. The $f(R)$ model predicts more halos for given initial conditions; however, the HOD equalizes the void size function so that it becomes consistent with GR. The HOD approximately normalizes the total number of tracers between the two theories when assigning mock galaxies, which in turn equalizes the number of voids identified with a watershed void finder.

The radial velocity v_r in all models has the same qualitative form, rising to a peak around the void edge and then tending to zero as one moves out away from the void. In both nDGP and $f(R)$ theories the radial velocity is enhanced relative to GR. In $f(R)$ the enhancement is most pronounced in smaller voids. While the magnitude of the increase in $v_{r,\mathrm{peak}}$ for $f(R)$ in HOD-identified voids is suppressed relative to those identified from all halos, the difference between GR and the two MG models remains present in voids of all sizes. The relative reduction in the velocity for $f(R)$ results from the HOD preferentially populating larger mass halos with mock galaxies, where these larger halos experience more chameleon screening compared to their smaller counterparts. In the N1 nDGP gravity model there is less scale dependence in the enhancements to the void peculiar velocity v_r, in accordance with the linearized nDGP field (16). The addition of a HOD has less impact; while the HOD still preferentially populates more massive halos, the shift symmetry present in (13) allows halos of all sizes to respond in a similar fashion to slowly varying background fields which source the fifth force [unlike $f(R)$ gravity]. Voids identified with halos and after the HOD is applied therefore yield similar enhancements to v_r from N1 gravity.

The velocity dispersion $\sigma_{v_\parallel}$ also has a common qualitative form in all models, being largely constant as one moves out from the void edge. The velocity dispersion is enhanced relative to GR in both the $f(R)$ and nDGP models, with ∼5% and 10% enhancements relative to GR, respectively, and in both cases has little dependence on void size.

Given the scale-dependent enhancements observed in v_r in the $f(R)$ model, we consider two size-based samples in our analyses, those above and below the median radius of $R_{\mathrm{eff}} = 35$ Mpc/h.

We perform a detailed analysis of the void quadruple moment ξ_2 to understand how sensitive redshift space statistics are to changes in the void dynamical properties within modified gravity. While we find increases in void velocity statistics of ∼5%–10% relative to GR in both void size populations and both modified theories, we find that changes to ξ_2 in both F5 or N1 are far more muted. For F5, the differences in velocities do not yield comparable

differences in ξ_2 to that in GR. In N1, we find a difference for the large void population of approximately 8% in ξ_2 in a limited region, 35–65 Mpc/h away from the void center.

We utilize the GSM to determine the origins of these findings. We first study the accuracy of the GSM in reproducing the redshift space void quadruple moment for modified gravity models. We find that the model is highly accurate in reproducing ξ_2, in both large- and small-size void samples and for both theories of modified gravity. We apply the model to understand how differences in the velocities and densities propagate to cause differences in ξ_2 in both modified gravity theories. Specifically, we isolate the changes induced in ξ_2 individually by δ^r, v_r, and $\sigma_{v_\parallel}$ using the first-order functional derivatives of the GSM.

In the functional derivative approach, the effects of Δv_r and $\Delta\sigma_{v_\parallel}$ on ξ_2 are opposite in sign and therefore act to counter each other in the same spatial region. Using this approach further, we find that changes to ξ_2 induced by changes to the line of sight velocity dispersion $\Delta\sigma_{v_\parallel}$ are found to be limited to the void edge region, despite that fact that the velocity dispersion continues to be enhanced at distances much further from the void center. The basis for this is that changes to ξ_2 cannot be driven by a constant $\Delta\sigma_{v_\parallel}$ unless the other GSM functions (primarily δ^r) simultaneously have nonzero radial gradients. Far from the void, all three GSM functions are slowly varying, which restricts changes induced in ξ_2 by the increased velocity dispersion to the void edge, where δ^r does have a large radial gradient. By contrast, the changes to ξ_2 induced by changes to the radial velocity Δv_r are not, in principle, confined to the area surrounding the void edge but instead extend throughout the entire region where Δv_r is nonzero. The spatial extent of Δv_r in both our $f(R)$ and nDGP model can be qualitatively related to the amount of screening present within the linearized field equations, (10) and (16), respectively. For $f(R)$, (10) experiences Yukawa screening, and, thus, Δv_r is short ranged and fails to extend far beyond the void edge. This in turn means that the changes induced in the quadrupole by Δv_r and $\Delta\sigma_{v_\parallel}$ are *both* confined to the same spatial region near the void edge and, being of opposite sign, cancel heavily and leave $\xi_{2,\mathrm{F5}}$ largely unchanged from $\xi_{2,\mathrm{GR}}$. On the other hand, in nDGP, (16) is unscreened at the linear level. This means that in nDGP gravity, particularly in the above-median size voids, that Δv_r has a large spatial range. For nDGP, therefore, the changes to $\Delta\xi_2$ induced by Δv_r and $\Delta\sigma_{v_\parallel}$ are *not* confined to the same spatial region and avoid substantial cancellation. This leads to differences arising between $\xi_{2,N1}$ and $\xi_{2,\mathrm{GR}}$ in the above-median size void population for $s \sim 35$–65 Mpc/h.

We translate differences between ξ_2 in each gravitational theory into constraints on the cosmological growth rate parameter β through the use of linear theory and the (β, σ_0) model. We find that within the large void population v_r can be accurately fit with linear theory, resulting in increased values of β for each modified gravity theory over the GR value. Although v_r is not an observable statistic, we can use it in the simulations to verify that a two-parameter fit to ξ_2 within the context of the GSM, with $v_r \propto \beta$ and $\sigma_{v_\parallel}(r) = \sigma_0$, can recover, in an unbiased manner, the same value of β as that recovered from v_r directly. Increased values of β are recovered in both $f(R)$ and nDGP gravitational scenarios.

When statistical uncertainties are computed corresponding to an observational volume of $\sim 1(\mathrm{Gpc/h})^3$ at $z = 0.5$, we find the values of β recovered from the ξ_2 fit in each modified gravity theory lie within the projected 1D error bars of the GR value. Applying this approach to an analysis of multiple redshift slices, akin to the full redshift range probed by upcoming spectroscopic surveys, will no doubt provide greater distinguishing power, although this is beyond the scope of this paper.

Our results show how the theoretical GSM model works remarkably well at modeling void dynamics in theories beyond GR. It also details, however, the challenges present in utilizing redshift space distortion data around cosmic voids to constrain the properties of gravity. The work also demonstrates the importance of considering the statistics derived from realistic HOD-derived tracers rather than the dark matter halos directly. We anticipate that the results from this paper will have broader applicability for accurately determining the constraining potential of cosmic voids for other nonstandard cosmological models.

ACKNOWLEDGMENTS

We wish to thank Baojiu Li and Cheng-Zong Ruan for kindly providing the MG-GLAM simulation products and providing advice and assistance in their use. The work of C. W. and R. B. is supported by National Science Foundation Grant No. AST 2206088, NASA ATP Grant No. 80NSSC18K0695, and NASA ROSES Grant No. 12-EUCLID12-0004.

APPENDIX: RESCALED ANALYSIS

In the main analysis we present results where the radial coordinate of the stacked voids is given in terms of the standard comoving distance, with units of comoving Mpc/h. Due to the symmetry properties of voids, there is a commonality in their density profiles when they are stacked using an alternative radial coordinate rescaled by each void's effective radius [112]. This rescaling allows voids to be conveniently stacked with each other in a way that draws on the void similarities and can alleviate effects caused by differences in void size when stacking voids of largely different R_{eff}.

In this appendix, we present results using this rescaled coordinate system as the partner results to those in the main text. The rescaled coordinates are defined as $\tilde{r} = r/R_{\mathrm{eff}}$ for physical space and $\tilde{s}$ in redshift space variables, with the relevant transformation being

$$\tilde{\mathbf{s}} = \tilde{\mathbf{r}} + \frac{\mathbf{v}\cdot\hat{\mathbf{l}}}{\mathcal{H}R_{\rm eff}}. \tag{A1}$$

When we perform the analysis binning tracers using the rescaled coordinates our definition of δ^r and δ^s slightly changes to reflect that, for voids of differing $R_{\rm eff}$, spherical slices at equal $\tilde{r}$ or $\tilde{s}$ are different sizes. Interpreting the term $N_v V(r)$ in the denominator of (20) as the "total volume averaged over," we use

$$\delta^{\tilde{r}}(\tilde{r}) = \frac{N_{vh}(\tilde{r})}{\bar{n}_h \sum_{\rm voids} V_i(\tilde{r})} - 1 \tag{A2}$$

and

$$\delta^{\tilde{s}}(\tilde{s},\mu_s) = \frac{N_{vh}(\tilde{s},\mu_s)}{\bar{n}_h \sum_{\rm voids} V_i(\tilde{s},\mu_s)} - 1, \tag{A3}$$

where $V_i(\tilde{s},\mu_s)$ is the volume (in unscaled space) of the bin at $(\tilde{s},\mu_s)$ in the ith void. For rescaled voids, we use 30 radial bins extending from 0 to $3R_{\rm eff}$ away from the void center, with the same angular binning as used in the unscaled analysis.

The Gaussian streaming model is also easily adapted for the purpose of analyzing redshift space distortions around rescaled voids. The only real differences from (24) are that $v_r \to v_r/R_{\rm eff} \equiv \tilde{v}_r$, $v_\parallel \to v_\parallel/R_{\rm eff} \equiv \tilde{v}_\parallel$, which then requires $\mathcal{P} \to \tilde{\mathcal{P}}$ with $\sigma_{v_\parallel} \to \sigma_{v_\parallel}/R_{\rm eff} \equiv \tilde{\sigma}_{v_\parallel}$. It should be noted that, in computing these quantities, each void rescales the velocities of its own tracers by its own $R_{\rm eff}$ before averaging to calculate $\tilde{v}_r$ and $\tilde{\sigma}_{v_\parallel}$.

Figures 8–13 show the rescaled counterparts to Figs. 2–7. The results obtained using the rescaled quantities are all consistent with those presented in the main text using unscaled quantities, although there are some differences

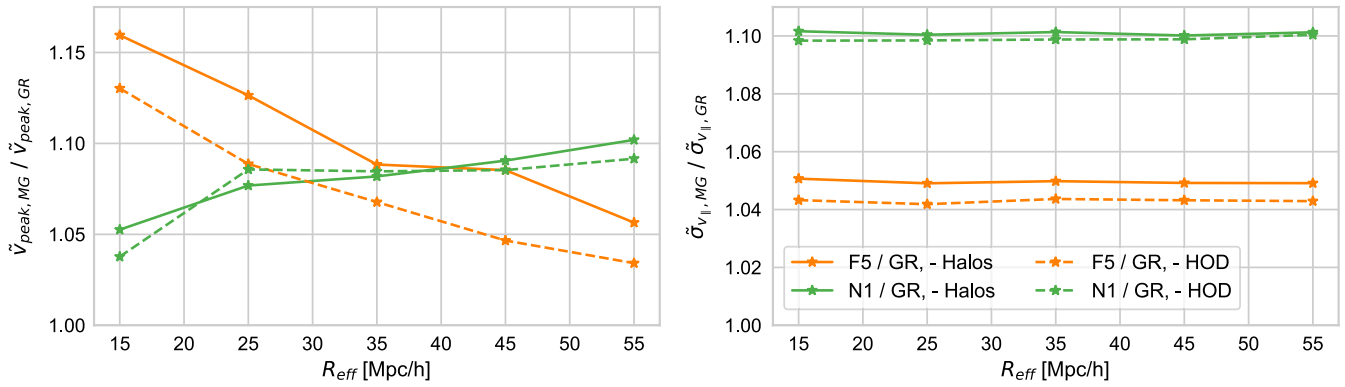

FIG. 8. Left: ratio of the peak rescaled radial velocity in F5 [orange] and N1 [green] to that in GR as a function of void effective radius $R_{\rm eff}$ for voids identified from halos [solid] and from halos containing mock galaxies identified by the HOD [dashed]. Right: ratio of the average asymptotic value of the rescaled velocity dispersion, at $\tilde{r} \gtrsim 1.5$, as a function of $R_{\rm eff}$.

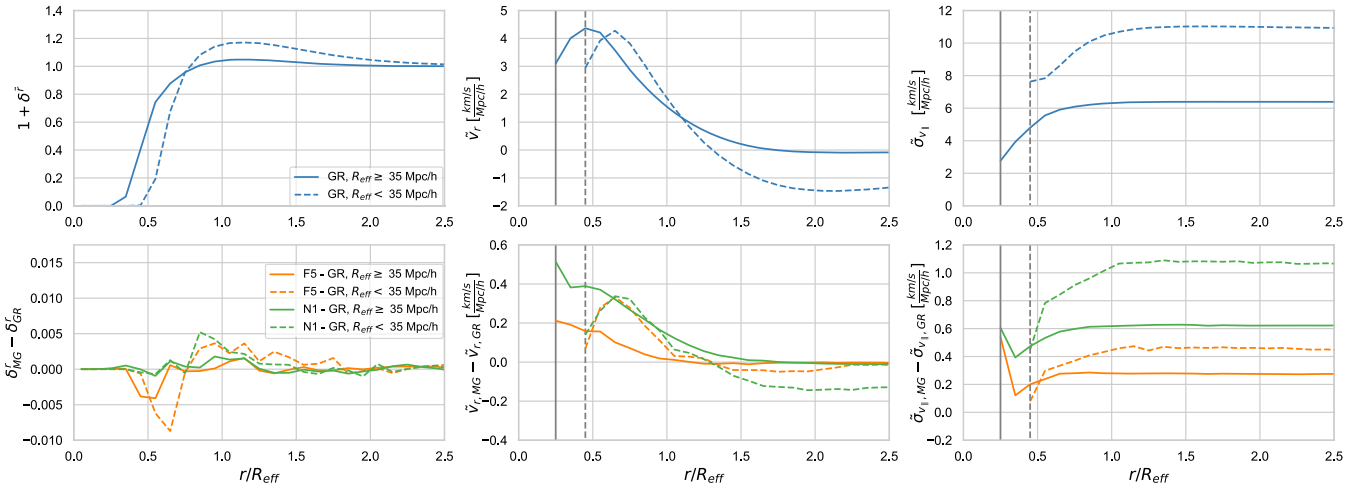

FIG. 9. Top row: void density [left], rescaled radial velocity [center] and rescaled velocity dispersion [right] profiles in GR for voids identified in halos with HOD-identified tracers. The void population is split into those with void size above [solid] and below [dashed] $R_{\rm eff} = 35$ Mpc/h, the median void size found in each of the three theories. Gray lines indicate the first radial bin below which no tracers are found. Bottom row: differences between F5 [orange] and N1 [green] quantities with respect to those in GR.

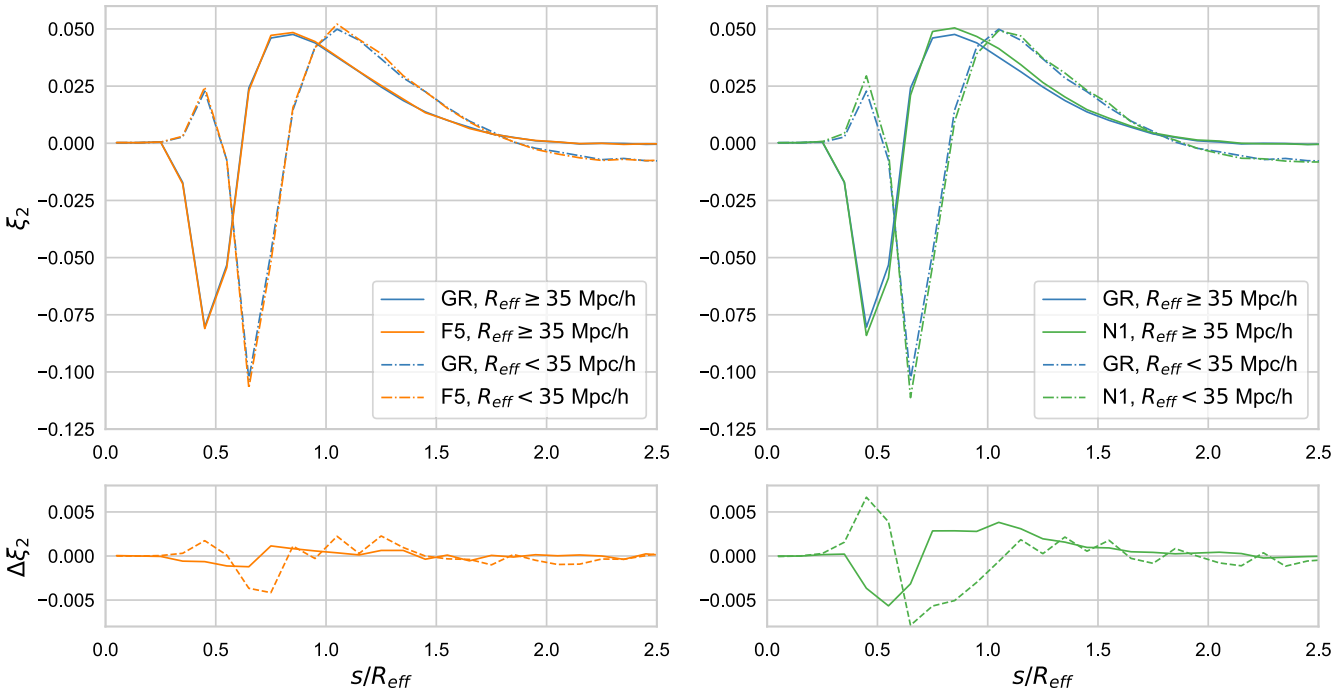

FIG. 10. Top Row: The void quadrupole moment ξ_2 at $z = 0.5$ for GR [blue] compared against F5 [left, orange] and N1 [right, green] in rescaled voids both below [dashed] and above [solid] the median void size. Bottom Row: Difference in ξ_2 between GR and each modified gravity theory in small [dashed] and large [solid] voids.

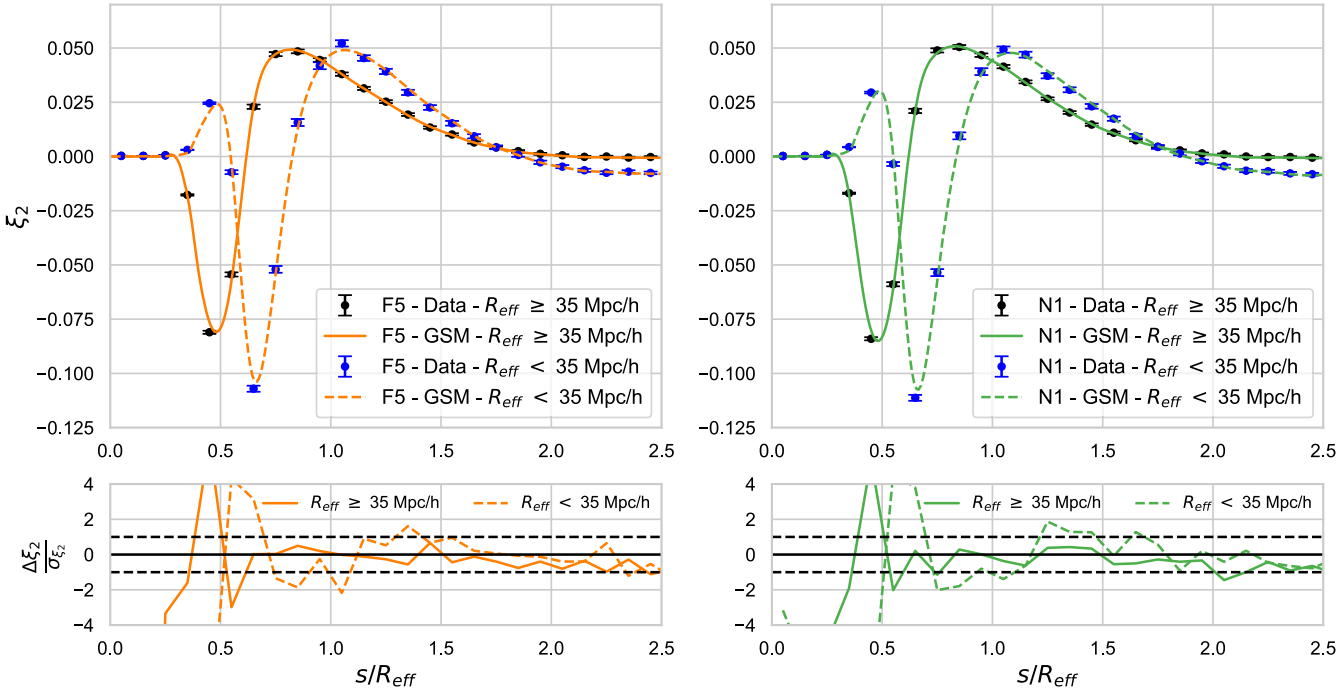

FIG. 11. Top: theoretical value of ξ_2 in rescaled voids both above [dashed] and below [solid] the median void size in F5 [left, orange] and N1 [right, green] calculated using the GSM compared to average ξ_2 from the simulations. Bottom: difference between the GSM-derived quadrupole and that from the simulated data, $\Delta\xi_2 = \xi_{2,\mathrm{GSM}} - \xi_{2,\mathrm{Data}}$, with respect to the statistical uncertainties for the model, σ_{ξ_2}.

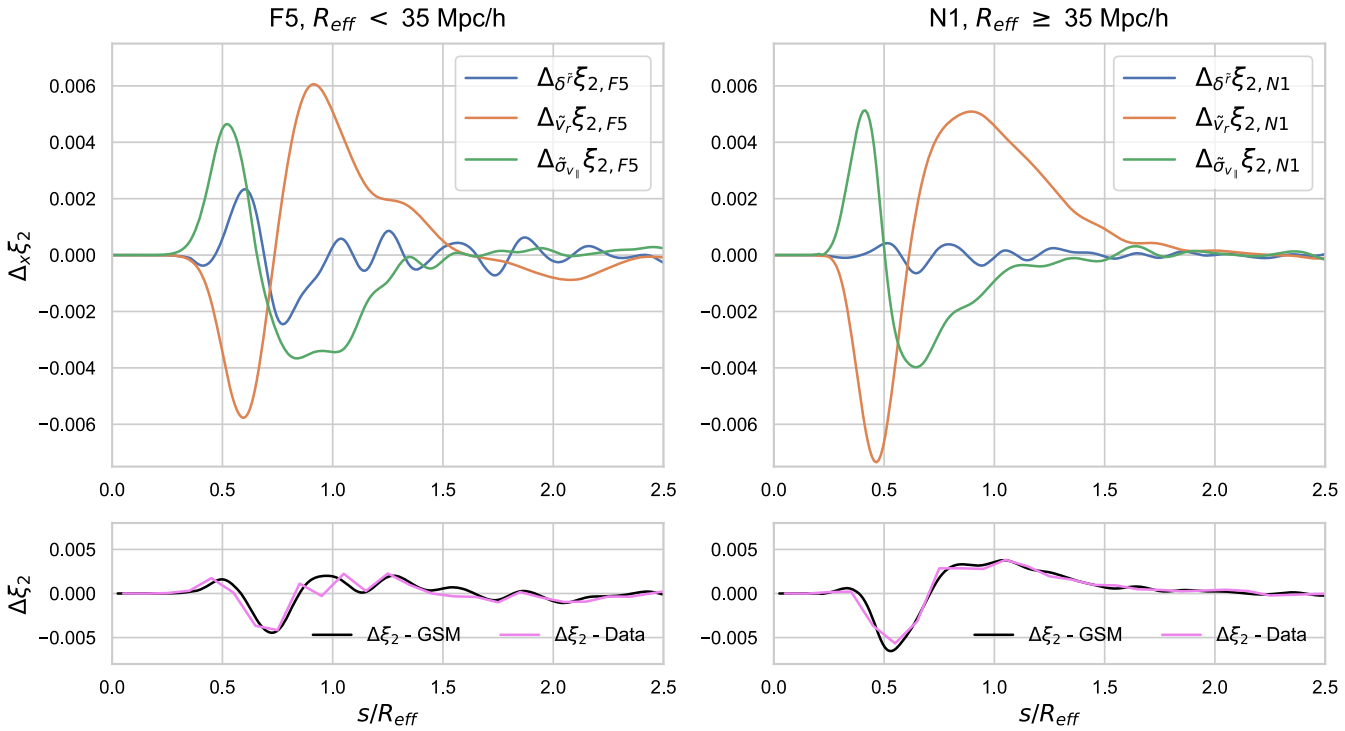

FIG. 12. Two scenarios are considered: [left] below-median size rescaled voids in F5 and [right] above-median size rescaled voids in N1. Top row: the changes to ξ_2 relative to GR induced independently by $\Delta\delta^{\tilde{r}}$ [blue], $\Delta\tilde{v}_r$ [orange], and $\Delta\tilde{\sigma}_{v_\parallel}$ [green] as calculated using GSM functional derivatives. Bottom row: comparison of the differences, $\Delta\xi_2$, between the modified gravity model and GR obtained from the simulated data in F5 [left, violet] and N1 [right, violet] and the summed GSM integrated functional derivatives [black].

caused by the rescalings which we comment on here, below.

Figure 8 shows the same patterns as shown in Fig. 2. Comparing the two figures, we can see that the effects caused by the transition from voids selected from halos to instead HOD mock galaxies are more clear when using rescaled variables.

Figure 9 shows the rescaled real space density profile $\delta^{\tilde{r}}(\tilde{r})$, the rescaled void radial velocity $\tilde{v}_r$, and the rescaled velocity dispersion profile. In Fig. 3, we saw that the unscaled v_r displayed a strong dependence on void size in $f(R)$, with its peak value increasing almost linearly with $R_{\rm eff}$ in accordance with linear theory. Concurrently, $\sigma_{v_\parallel}$ was independent of $R_{\rm eff}$ and plateaued to the same value for both small and large voids. In Fig. 9, with rescaled quantities, these properties are reversed. Dividing by a factor of $R_{\rm eff}$ effectively makes $\tilde{v}_r$ scale independent, with differences in $\tilde{v}_r$ instead coming from differences in $\delta^{\tilde{r}}(\tilde{r})$ and not differences in $R_{\rm eff}$ between the two void populations. Whereas previously $\sigma_{v_\parallel}$ was scale independent, dividing by $R_{\rm eff}$ introduces scale dependence in $\tilde{\sigma}_{v_\parallel}$, causing smaller voids, which divide by a smaller $R_{\rm eff}$, to have larger values of $\tilde{\sigma}_{v_\parallel}$ than larger voids.

The bottom row of Fig. 9 shows the spatial extent of $\Delta\tilde{v}_r$ is consistent with that of the unscaled Δv_r. $\Delta\tilde{v}_r$ extends out past $1.5\tilde{r}$ in the large N1 voids and is more confined, to $\tilde{r} < 1$, in both the large and small radius F5 void samples.

Figure 10 shows that the trends in the void quadrupole moments for rescaled coordinates are the same as seen for unscaled coordinates in Fig. 4 in both the large and small void populations in each of the three theories of gravity considered.

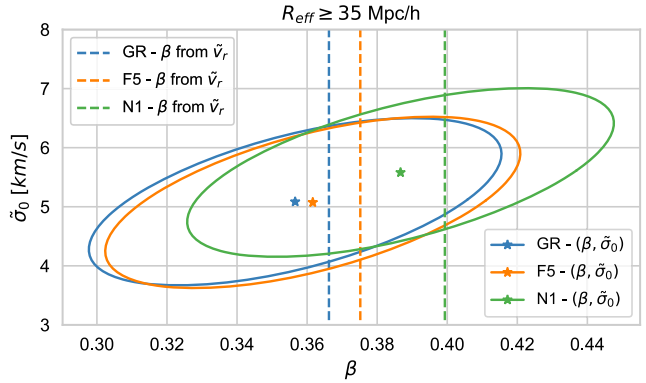

FIG. 13. The linear growth rate dependent parameter β, calculated from $\tilde{v}_r$ directly using linear theory [dashed lines], compared with the best fit [star] and the 68% confidence ellipses [full line] from ξ_2 modeled using the GSM with the $(\beta, \tilde{\sigma}_0)$ parametrization, in GR [blue], F5 [orange], and N1 [green]. The model is fit to the mean quadrupole from 100 realizations for the above-median size void sample with confidence ellipses derived from statistical uncertainties estimated for one realization, with volume $(1.024\ \mathrm{Gpc/h})^3$.

Figures 11 and 12 demonstrate that the GSM approach and functional derivative analysis can be accurately used to predict the quadrupole using rescaled quantities across both void populations and all theories of gravity (GR not shown).

In order to reproduce Fig. 7 for rescaled voids, we fit $\tilde{v}_r$ with linear theory. The rescaling slightly modifies (35), so that for $\tilde{v}_r$, we have

$$\tilde{v}_r(\tilde{r}) = -\frac{\beta}{3}\mathcal{H}\Delta_{gal}(\tilde{r})\tilde{r}, \tag{A4}$$

$$\Delta_{gal}(\tilde{r}) \equiv \frac{1}{\frac{4}{3}\pi\tilde{r}^3}\int_0^{\tilde{r}} 4\pi\delta^r_{gal}(\tilde{r}')\tilde{r}'^2 d\tilde{r}', \tag{A5}$$

where $\delta^{\tilde{r}}(\tilde{r})$ is computed as in (A2).

Figure 13 shows the confidence ellipses for $(\beta, \tilde{\sigma}_0)$ from rescaled voids in GR, F5, and N1, as well as the best-fit values of β calculated directly from fitting (A5) to the true rescaled radial velocity profile $\tilde{v}_r$. There is only a slight difference between the vertical lines shown in Fig. 13 and those in Fig. 7, indicating consistency in the methods used to calculate v_r and $\tilde{v}_r$ from linear theory. When comparing scaled versus unscaled, the recovered β from the (β, σ_0) fit is closer to the "true" value in unscaled voids (Fig. 7), although both are well within the 1σ confidence ellipse for all three theories of gravity. The difference arise due to the $\sigma_{v_\parallel}(r) = \sigma_0$ assumption providing a better fit to the true $\sigma_{v_\parallel}(r)$ profile in unscaled voids compared to rescaled ones (Fig. 3 vs 9).

[1] S. Perlmutter *et al.* (Supernova Cosmology Project), Astrophys. J. **517**, 565 (1999).
[2] A. G. Riess *et al.* (Supernova Search Team), Astrophys. J. **607**, 665 (2004).
[3] D. J. Eisenstein *et al.* (SDSS Collaboration), Astrophys. J. **633**, 560 (2005).
[4] W. J. Percival, S. Cole, D. J. Eisenstein, R. C. Nichol, J. A. Peacock, A. C. Pope, and A. S. Szalay, Mon. Not. R. Astron. Soc. **381**, 1053 (2007).
[5] W. J. Percival *et al.*, Mon. Not. R. Astron. Soc. **401**, 2148 (2010).
[6] E. A. Kazin, J. Koda, C. Blake, and N. Padmanabhan, Mon. Not. R. Astron. Soc. **441**, 3524 (2014).
[7] D. Spergel, N. Gehrels, J. Breckinridge, M. Donahue, A. Dressler *et al.*, arXiv:1305.5422.
[8] P. Ade *et al.* (Planck Collaboration), Astron. Astrophys. **571**, A16 (2014).
[9] P. A. R. Ade *et al.* (Planck Collaboration), Astron. Astrophys. **594**, A13 (2016).
[10] T. Clifton, P. G. Ferreira, A. Padilla, and C. Skordis, Phys. Rep. **513**, 1 (2012).
[11] C. M. Will, Living Rev. Relativity **9**, 3 (2006).
[12] W. Hu and I. Sawicki, Phys. Rev. D **76**, 064004 (2007).
[13] J. Khoury and A. Weltman, Phys. Rev. Lett. **93**, 171104 (2004).
[14] J. Khoury and A. Weltman, Phys. Rev. D **69**, 044026 (2004).
[15] G. Dvali, G. Gabadadze, and M. Porrati, Phys. Lett. B **485**, 208 (2000).
[16] A. Vainshtein, Phys. Lett. **39B**, 393 (1972).
[17] C. Sánchez, J. Clampitt, A. Kovacs, B. Jain, J. García-Bellido, S. Nadathur, D. Gruen, N. Hamaus, D. Huterer, P. Vielzeuf *et al.*, Mon. Not. R. Astron. Soc. **465**, 746 (2016).
[18] P. M. Sutter, G. Lavaux, B. D. Wandelt, D. H. Weinberg, M. S. Warren, and A. Pisani, Mon. Not. R. Astron. Soc. **442**, 3127 (2014).
[19] A. J. Hawken, M. Aubert, A. Pisani, M.-C. Cousinou, S. Escoffier, S. Nadathur, G. Rossi, and D. P. Schneider, J. Cosmol. Astropart. Phys. 06 (**2020**) 012.
[20] A. Kovács, P. Vielzeuf, I. Ferrero, P. Fosalba, U. Demirbozan, R. Miquel, C. Chang, N. Hamaus, G. Pollina, K. Bechtol *et al.*, Mon. Not. R. Astron. Soc. **515**, 4417 (2022).
[21] E. Krause, T.-C. Chang, O. Dore, and K. Umetsu, Astrophys. J. Lett. **762**, L20 (2013).
[22] T. Chantavat, U. Sawangwit, P. Sutter, and B. D. Wandelt, Phys. Rev. D **93**, 043523 (2016).
[23] C. T. Davies, M. Cautun, and B. Li, Mon. Not. R. Astron. Soc. **480**, L101 (2018).
[24] C. T. Davies, M. Cautun, B. Giblin, B. Li, J. Harnois-Déraps, and Y.-C. Cai, Mon. Not. R. Astron. Soc. **507**, 2267 (2021).
[25] S. Raghunathan, S. Nadathur, B. D. Sherwin, and N. Whitehorn, Astrophys. J. **890**, 168 (2020).
[26] P. Melchior, P. M. Sutter, E. S. Sheldon, E. Krause, and B. D. Wandelt, Mon. Not. R. Astron. Soc. **440**, 2922 (2014).
[27] J. Clampitt and B. Jain, Mon. Not. R. Astron. Soc. **454**, 3357 (2015).
[28] Y. Fang, N. Hamaus, B. Jain, S. Pandey, G. Pollina, C. Sánchez, A. Kovács, C. Chang, J. Carretero, F. J. Castander *et al.*, Mon. Not. R. Astron. Soc. **490**, 3573 (2019).
[29] M. Bonici, C. Carbone, S. Davini, P. Vielzeuf, L. Paganin, V. Cardone, N. Hamaus, A. Pisani, A. J. Hawken, A. Kovacs *et al.*, Astron. Astrophys. **670**, A47 (2023).
[30] N. Hamaus, P. Sutter, G. Lavaux, and B. D. Wandelt, J. Cosmol. Astropart. Phys. 11 (**2015**) 036.
[31] N. Hamaus, A. Pisani, P. M. Sutter, G. Lavaux, S. Escoffier, B. D. Wandelt, and J. Weller, Phys. Rev. Lett. **117**, 091302 (2016).
[32] Y.-C. Cai, A. Taylor, J. A. Peacock, and N. Padilla, Mon. Not. R. Astron. Soc. **462**, 2465 (2016).

[33] S. Nadathur and W. J. Percival, Mon. Not. R. Astron. Soc. **483**, 3472 (2019).
[34] C.-H. Chuang, F.-S. Kitaura, Y. Liang, A. Font-Ribera, C. Zhao, P. McDonald, and C. Tao, Phys. Rev. D **95**, 063528 (2017).
[35] D. Sakuma, A. Terukina, K. Yamamoto, and C. Hikage, Phys. Rev. D **97**, 063512 (2018).
[36] S. Nadathur, P. M. Carter, W. J. Percival, H. A. Winther, and J. E. Bautista, Phys. Rev. D **100**, 023504 (2019).
[37] C. M. Correa, D. J. Paz, A. G. Sánchez, A. N. Ruiz, N. D. Padilla, and R. E. Angulo, Mon. Not. R. Astron. Soc. **500**, 911 (2020).
[38] S. Nadathur, A. Woodfinden, W. J. Percival, M. Aubert, J. Bautista, K. Dawson, S. Escoffier, S. Fromenteau, H. Gil-Marín, J. Rich *et al.*, Mon. Not. R. Astron. Soc. **499**, 4140 (2020).
[39] D. Paz, M. Lares, L. Ceccarelli, N. Padilla, and D. G. Lambas, Mon. Not. R. Astron. Soc. **436**, 3480 (2013).
[40] I. Achitouv, Phys. Rev. D **100**, 123513 (2019).
[41] N. Hamaus, A. Pisani, J.-A. Choi, G. Lavaux, B. D. Wandelt, and J. Weller, J. Cosmol. Astropart. Phys. 12 (2020) 023.
[42] Y.-C. Cai, M. Neyrinck, Q. Mao, J. A. Peacock, I. Szapudi, and A. A. Berlind, Mon. Not. R. Astron. Soc. **466**, 3364 (2017).
[43] A. Kovács *et al.* (DES Collaboration), Mon. Not. R. Astron. Soc. **515**, 4417 (2022).
[44] S. Nadathur, S. Hotchkiss, and S. Sarkar, J. Cosmol. Astropart. Phys. 06 (2012) 042.
[45] S. Nadathur and R. Crittenden, Astrophys. J. Lett. **830**, L19 (2016).
[46] B. R. Granett, M. C. Neyrinck, and I. Szapudi, Astrophys. J. **683**, L99 (2008).
[47] S. Ilić, M. Langer, and M. Douspis, Astron. Astrophys. **556**, A51 (2013).
[48] Y.-C. Cai, M. C. Neyrinck, I. Szapudi, S. Cole, and C. S. Frenk, Astrophys. J. **786**, 110 (2014).
[49] A. Kovács, C. Sánchez, J. García-Bellido, J. Elvin-Poole, N. Hamaus, V. Miranda, S. Nadathur, T. Abbott, F. B. Abdalla, J. Annis *et al.*, Mon. Not. R. Astron. Soc. **484**, 5267 (2019).
[50] Y.-C. Li, Y.-Z. Ma, and S. Nadathur, arXiv:2002.01689.
[51] N. Hamaus, M. Aubert, A. Pisani, S. Contarini, G. Verza, M.-C. Cousinou, S. Escoffier, A. Hawken, G. Lavaux, G. Pollina *et al.*, Astron. Astrophys. **658**, A20 (2022).
[52] M. E. Levi, L. E. Allen, A. Raichoor, C. Baltay, S. BenZvi, F. Beutler, A. Bolton, F. J. Castander, C.-H. Chuang, A. Cooper *et al.*, arXiv:1907.10688.
[53] A. Aghamousa, J. Aguilar, S. Ahlen, S. Alam, L. E. Allen, C. Allende Prieto, J. Annis, S. Bailey, C. Balland *et al.* (DESI Collaboration), arXiv:1611.00036.
[54] Ž. Ivezić, S. M. Kahn, J. A. Tyson, B. Abel, E. Acosta, R. Allsman, D. Alonso, Y. AlSayyad, S. F. Anderson, J. Andrew *et al.*, Astrophys. J. **873**, 111 (2019).
[55] D. Spergel, N. Gehrels, C. Baltay, D. Bennett, J. Breckinridge, M. Donahue, A. Dressler, B. S. Gaudi, T. Greene, O. Guyon *et al.*, arXiv:1503.03757.
[56] P. Ade, J. Aguirre, Z. Ahmed, S. Aiola, A. Ali, D. Alonso, M. A. Alvarez, K. Arnold, P. Ashton, J. Austermann *et al.*, J. Cosmol. Astropart. Phys. 02 (2019) 056.
[57] K. N. Abazajian, P. Adshead, Z. Ahmed, S. W. Allen, D. Alonso, K. S. Arnold, C. Baccigalupi, J. G. Bartlett, N. Battaglia, B. A. Benson *et al.*, arXiv:1610.02743.
[58] R. Sheth and R. Weygaert, Mon. Not. R. Astron. Soc. **350**, 517 (2004).
[59] A. Pisani, P. Sutter, N. Hamaus, E. Alizadeh, R. Biswas, B. D. Wandelt, and C. M. Hirata, Phys. Rev. D **92**, 083531 (2015).
[60] R. Wojtak, D. Powell, and T. Abel, Mon. Not. R. Astron. Soc. **458**, 4431 (2016).
[61] E. Adermann, P. J. Elahi, G. F. Lewis, and C. Power, Mon. Not. R. Astron. Soc. **468**, 3381 (2017).
[62] S. Contarini, T. Ronconi, F. Marulli, L. Moscardini, A. Veropalumbo, and M. Baldi, Mon. Not. R. Astron. Soc. **488**, 3526 (2019).
[63] L. Ceccarelli, D. Paz, M. Lares, N. Padilla, and D. G. Lambas, Mon. Not. R. Astron. Soc. **434**, 1435 (2013).
[64] E. Ricciardelli, V. Quilis, and J. Varela, Mon. Not. R. Astron. Soc. **440**, 601 (2014).
[65] B. Novosyadlyj, M. Tsizh, and Y. Kulinich, Mon. Not. R. Astron. Soc. **465**, 482 (2017).
[66] E. Massara and R. K. Sheth, arXiv:1811.03132.
[67] M. Aragon-Calvo and A. Szalay, Mon. Not. R. Astron. Soc. **428**, 3409 (2013).
[68] D. G. Lambas, M. Lares, L. Ceccarelli, A. N. Ruiz, D. J. Paz, V. E. Maldonado, and H. E. Luparello, Mon. Not. R. Astron. Soc. **455**, L99 (2016).
[69] E. Adermann, P. J. Elahi, G. F. Lewis, and C. Power, Mon. Not. R. Astron. Soc. **479**, 4861 (2018).
[70] S. Nadathur, W. J. Percival, F. Beutler, and H. A. Winther, Phys. Rev. Lett. **124**, 221301 (2020).
[71] G. Verza, A. Pisani, C. Carbone, N. Hamaus, and L. Guzzo, J. Cosmol. Astropart. Phys. 12 (2019) 040.
[72] J. Lee and D. Park, Astrophys. J. **696**, L10 (2009).
[73] N. Schuster, N. Hamaus, A. Pisani, C. Carbone, C. D. Kreisch, G. Pollina, and J. Weller, J. Cosmol. Astropart. Phys. 12 (2019) 055.
[74] E. Massara, F. Villaescusa-Navarro, M. Viel, and P. Sutter, J. Cosmol. Astropart. Phys. 11 (2015) 018.
[75] C. D. Kreisch, A. Pisani, C. Carbone, J. Liu, A. J. Hawken, E. Massara, D. N. Spergel, and B. D. Wandelt, Mon. Not. R. Astron. Soc. **488**, 4413 (2019).
[76] A. E. Bayer, F. Villaescusa-Navarro, E. Massara, J. Liu, D. N. Spergel, L. Verde, B. D. Wandelt, M. Viel, and S. Ho, Astrophys. J. **919**, 24 (2021).
[77] E. L. D. Perico, R. Voivodic, M. Lima, and D. F. Mota, Astron. Astrophys. **632**, A52 (2019).
[78] C. Wilson and R. Bean, Phys. Rev. D **104**, 023512 (2021).
[79] B. Li, G.-B. Zhao, and K. Koyama, Mon. Not. R. Astron. Soc. **421**, 3481 (2012).
[80] P. Zivick, P. Sutter, B. D. Wandelt, B. Li, and T. Y. Lam, Mon. Not. R. Astron. Soc. **451**, 4215 (2015).
[81] E. Perico, R. Voivodic, M. Lima, and D. Mota, Astron. Astrophys. **632**, A52 (2019).
[82] S. Contarini, F. Marulli, L. Moscardini, A. Veropalumbo, C. Giocoli, and M. Baldi, Mon. Not. R. Astron. Soc. **504**, 5021 (2021).
[83] N. Padilla, D. Paz, M. Lares, L. Ceccarelli, D. G. Lambas, Y.-C. Cai, and B. Li, IAU Symp. **308**, 530 (2014).

[84] Y.-C. Cai, N. Padilla, and B. Li, Mon. Not. R. Astron. Soc. **451**, 1036 (2015).
[85] C. T. Davies, M. Cautun, and B. Li, Mon. Not. R. Astron. Soc. **490**, 4907 (2019).
[86] B. Falck, K. Koyama, G.-B. Zhao, and M. Cautun, Mon. Not. R. Astron. Soc. **475**, 3262 (2018).
[87] E. Paillas, M. Cautun, B. Li, Y.-C. Cai, N. Padilla, J. Armijo, and S. Bose, Mon. Not. R. Astron. Soc. **484**, 1149 (2019).
[88] T. Baker, J. Clampitt, B. Jain, and M. Trodden, Phys. Rev. D **98**, 023511 (2018).
[89] A. Barreira, M. Cautun, B. Li, C. Baugh, and S. Pascoli, J. Cosmol. Astropart. Phys. 08 (**2015**) 028.
[90] N. Hamaus, M.-C. Cousinou, A. Pisani, M. Aubert, S. Escoffier, and J. Weller, J. Cosmol. Astropart. Phys. 07 (2017) 014.
[91] S. Nojiri and S. D. Odintsov, Phys. Rev. D **74**, 086005 (2006).
[92] K. Koyama and F. P. Silva, Phys. Rev. D **75**, 084040 (2007).
[93] M. A. Mitchell, C. Hernández-Aguayo, C. Arnold, and B. Li, Mon. Not. R. Astron. Soc. **508**, 4140 (2021).
[94] A. Klypin and F. Prada, Mon. Not. R. Astron. Soc. **478**, 4602 (2018).
[95] C.-Z. Ruan, C. Hernández-Aguayo, B. Li, C. Arnold, C. M. Baugh, A. Klypin, and F. Prada, J. Cosmol. Astropart. Phys. 05 (2022) 018.
[96] C. Hernández-Aguayo, C.-Z. Ruan, B. Li, C. Arnold, C. M. Baugh, A. Klypin, and F. Prada, J. Cosmol. Astropart. Phys. 01 (2022) 048.
[97] P. A. R. Ade, N. Aghanim, M. Arnaud, M. Ashdown, J. Aumont, C. Baccigalupi, A. J. Banday, R. B. Barreiro, J. G. Bartlett, N. Bartolo *et al.*, Astron. Astrophys. **594**, A13 (2016).
[98] Y. B. Zel'dovich, Astron. Astrophys. **5**, 84 (1970).
[99] A. Klypin and J. Holtzman, arXiv:astro-ph/9712217.
[100] L. Baojiu and R. Cheng-Zong (private communication).
[101] B. Falck, K. Koyama, and G.-B. Zhao, J. Cosmol. Astropart. Phys. 07 (2015) 049.
[102] C. Hernández-Aguayo, C. M. Baugh, and B. Li, Mon. Not. R. Astron. Soc. **479**, 4824 (2018).
[103] A. A. Berlind, D. H. Weinberg, A. J. Benson, C. M. Baugh, S. Cole, R. Dave, C. S. Frenk, A. Jenkins, N. Katz, and C. G. Lacey, Astrophys. J. **593**, 1 (2003).
[104] Z. Zheng, A. A. Berlind, D. H. Weinberg, A. J. Benson, C. M. Baugh, S. Cole, R. Dave, C. S. Frenk, N. Katz, and C. G. Lacey, Astrophys. J. **633**, 791 (2005).
[105] Z. Zheng, A. L. Coil, and I. Zehavi, Astrophys. J. **667**, 760 (2007).
[106] S. Alam, A. Aviles, R. Bean, Y.-C. Cai, M. Cautun, J. L. Cervantes-Cota, C. Cuesta-Lazaro, N. C. Devi, A. Eggemeier, S. Fromenteau *et al.*, J. Cosmol. Astropart. Phys. 11 (2021) 050.
[107] M. Manera, R. Scoccimarro, W. J. Percival, L. Samushia, C. K. McBride, A. J. Ross, R. K. Sheth, M. White, B. A. Reid, A. G. Sánchez *et al.*, Mon. Not. R. Astron. Soc. **428**, 1036 (2012).
[108] P. Sutter, G. Lavaux, N. Hamaus, A. Pisani, B. D. Wandelt, M. S. Warren, F. Villaescusa-Navarro, P. Zivick, Q. Mao, and B. B. Thompson, Astron. Comput. **9**, 1 (2015).
[109] M. C. Neyrinck, Mon. Not. R. Astron. Soc. **386**, 2101 (2008).
[110] S. Nadathur and S. Hotchkiss, Mon. Not. R. Astron. Soc. **454**, 2228 (2015).
[111] S. Nadathur, S. Hotchkiss, and R. Crittenden, Mon. Not. R. Astron. Soc. **467**, 4067 (2017).
[112] N. Hamaus, P. Sutter, and B. D. Wandelt, Phys. Rev. Lett. **112**, 251302 (2014).
[113] P. J. E. Peebles, *The Large-Scale Structure of the Universe* (Princeton University Press, Princeton, New Jersey, 1980).
[114] K. B. Fisher, Astrophys. J. **448**, 494 (1995).
[115] E. Paillas, Y.-C. Cai, N. Padilla, and A. G. Sánchez, Mon. Not. R. Astron. Soc. **505**, 5731 (2021).
[116] E. Jennings, Y. Li, and W. Hu, Mon. Not. R. Astron. Soc. **434**, 2167 (2013).
[117] N. Schuster, N. Hamaus, K. Dolag, and J. Weller, arXiv:2210.02457.
[118] D. Shi, B. Li, and J. Han, Mon. Not. R. Astron. Soc. **469**, 705 (2017).
[119] B. Falck, K. Koyama, G. bo Zhao, and B. Li, J. Cosmol. Astropart. Phys. 07 (2014) 058.
[120] L. Hui, A. Nicolis, and C. W. Stubbs, Phys. Rev. D **80**, 104002 (2009).
[121] W. A. Hellwing, A. Barreira, C. S. Frenk, B. Li, and S. Cole, Phys. Rev. Lett. **112**, 221102 (2014).
[122] B. Fiorini, K. Koyama, and A. Izard, J. Cosmol. Astropart. Phys. 12 (2022) 028.